



Titre: Numerical simulation of merging of two rising bubbles with different densities and diameters using an enhanced Volume-Of-Fluid (VOF) model
Title:

Auteurs: Faroogh Garoosi, Tarek Merabtene, & Tew-Fik Mahdi
Authors:

Date: 2022

Type: Article de revue / Article

Référence: Garoosi, F., Merabtene, T., & Mahdi, T.-F. (2022). Numerical simulation of merging of two rising bubbles with different densities and diameters using an enhanced Volume-Of-Fluid (VOF) model. *Ocean Engineering*, 247, 110711 (27 pages).
Citation: <https://doi.org/10.1016/j.oceaneng.2022.110711>

 **Document en libre accès dans PolyPublie**
Open Access document in PolyPublie

URL de PolyPublie: <https://publications.polymtl.ca/10169/>
PolyPublie URL:

Version: Version finale avant publication / Accepted version
Révisé par les pairs / Refereed

Conditions d'utilisation: CC BY-NC-ND
Terms of Use:

 **Document publié chez l'éditeur officiel**
Document issued by the official publisher

Titre de la revue: Ocean Engineering (vol. 247)
Journal Title:

Maison d'édition: Elsevier
Publisher:

URL officiel: <https://doi.org/10.1016/j.oceaneng.2022.110711>
Official URL:

Mention légale: © 2022. This is the author's version of an article that appeared in Ocean Engineering (vol. 247) . The final published version is available at <https://doi.org/10.1016/j.oceaneng.2022.110711>. This manuscript version is made available under the CC-BY-NC-ND 4.0 license <https://creativecommons.org/licenses/by-nc-nd/4.0/>
Legal notice:

1
2
3
4 **Numerical simulation of merging of two rising bubbles with different densities and**
5 **diameters using an enhanced Volume-Of-Fluid (VOF) model**
6
7

8
9 Faroogh Garoosi^{*,a}, Tarek Merabtene^b, Tew-Fik Mahdi^a

10
11 ^aDepartment of Civil, Geological and Mining Engineering, Polytechnique Montreal, Montreal,
12 Quebec, Canada
13

14
15 ^bDepartment of Civil and Environmental Engineering, University of Sharjah. P. O.Box 27272
16 Sharjah. United Arab Emirates
17

18 *Corresponding author: faroogh.garoosi@polymtl.ca,*

19
20 *Second author: tmerabtene@sharjah.ac.ae*

21
22 *Third author: tewfik.mahdi@polymtl.ca*
23
24

25 **Abstract**
26

27
28 In this study, the transient evolution of two rising bubbles with different densities is investigated
29 numerically using an enhanced version of the VOF model, aiming to establish an state-of-the-art
30 benchmark solutions and up-to-date data set for CFD validations. The simulations are performed
31 on the staggered grid system where a novel third- order accurate monotone convection scheme is
32 applied for the discretization of the convection terms in Navier-Stokes and volume fraction
33 equations while the semi-iterative PISOC algorithm (a combined version of the classical PISO
34 and Chorin's model) are used to solve the pressure-velocity coupling. To reduce the false
35 diffusion errors and mitigate smearing of interface thickness in the regions of physical
36 discontinuities, the interface compression technique is also incorporated into the transport
37 equation. To further enhance the accuracy of the numerical solutions, the idea of Piecewise
38 Linear Interface Calculation (PLIC) based on the ELVIRA technique (Efficient Least-square
39 Volume-of-fluid Interface Reconstruction Algorithm) is also utilized for the interface
40 reconstruction and accurate implementation of surface tension force. The validity and accuracy
41 of the enhanced VOF model is further demonstrated against a series of challenging benchmark
42
43
44
45
46
47
48
49
50
51
52
53
54
55
56
57
58
59
60
61

1
2
3
4 cases including draining of liquids from the storage tank (tank draining), single rising bubble,
5
6 three-phase Rayleigh-Taylor Instability and dam-break flows over dry and wet beds. The
7
8 comparison of the obtained results with previously published data vividly demonstrates the
9
10 superiority of the proposed method over the standard VOF/Level-Set models in handling
11
12 multiphase/multi-fluid flow problems with large topological changes. In the last stage, the
13
14 morphology and hydrodynamic characteristics of merging of two rising bubbles with different
15
16 densities and diameters are examined and analyzed in details. The results show that, the
17
18 initial/final deformations and the subsequent steady-state rise of two bubbles are remarkably
19
20 influenced by the diameters of leading (upper) and trailing (lower) bubbles.
21
22
23
24
25
26

27 **Keywords:** Monotone convection scheme; PISOC algorithm; Multiphase flows; VOF model;
28 merging of two rising bubbles;
29
30

31 **Nomenclature**

34	C_ϕ	Interface compression coefficient
35	F_g	gravity force
36	F_{ST}	surface tension force
37	g	Gravitational acceleration, ms^{-2}
38	H	enclosure height, m
39	L	Length of the enclosure (m)
40	\mathbf{n}	interface normal vector
41	p	pressure, Nm^{-2}
42	P	dimensionless pressure
43	t	time (s)
44	t^*	dimensionless time, $(t\alpha/H^2)$
45	u, v	velocity components, ms^{-1}
46	\mathbf{u}_R	artificial compressive velocity, ms^{-1}

Re	Reynolds number
U, V	Dimensionless velocity components
x, y	Cartesian coordinates, m
X, Y	Dimensionless Cartesian coordinates
We	Weber number

Greek symbols

μ	dynamic viscosity, $\text{kg m}^{-1} \text{s}^{-1}$
ν	kinematic viscosity, m^2s^{-1}
ρ	density, kg m^{-3}
φ	Volume fraction of the primary phase (phase 1)
λ	Volume fraction of the secondary phase (phase 2)
γ	Volume fraction of the third phase (phase 3)
k	curvature of interface
σ	interfacial tension coefficient, kg s^{-2}
ψ	stream function($= -\int_{Y_0}^Y U \partial Y + \psi(X, Y_0)$)

Subscripts

L	Lighter fluid
H	Heavy fluid
M	Middle fluid

1. Introduction

Multiphase flows where two or more immiscible fluids exist simultaneously in a domain are ubiquitous in a wide range of industrial and natural processes including fluidized beds [1,2], tsunami propagation [3–5], droplet impact [6,7], sediment transport [8,9], landslides and impulse waves [10]. The utilization of numerical methodologies as a promising cost-effective alternatives to conventional experimental and theoretical approaches has received a great deal of attention

1
2
3
4 during the last two decades [11]. However, the accurate tracking or capturing of the moving
5
6 interfaces, together with the complex interface dynamics (i.e. coalescence or segregation) and
7
8 discontinuous variations of material properties that frequently characterize such phenomena,
9
10 impose tremendous challenges on numerical modelling [12]. Fundamentally, interface-resolved
11
12 simulations of multiphase flows can be differentiated into two distinct categories according to
13
14 the interface representation namely: (I) interface-tracking, and (II) interface-capturing methods
15
16 [13,14]. With the former approach, the position of the material discontinuities is explicitly
17
18 determined by a set of mobile particles attached to the interface (Lagrangian markers). Examples
19
20 include Arbitrary-Lagrangian Eulerian (ALE) [15], front-tracking [16] and point-set method
21
22 [17]. However, these models are computationally expensive and needs regular particle
23
24 rearrangement (or re-meshing) especially when the interface is stretched or compressed [18].
25
26 Methods that fall in the second class are the Level-Set, (LS) [19] and the Volume-Of-Fluid
27
28 (VOF) [20] in which an auxiliary scalar partial differential equation (PDE) is implicitly solved to
29
30 represent the interface profile. Given the pros and cons of both methods, LS and VOF have been
31
32 extensively applied to a broad range of engineering problems such as atomization and
33
34 solidification [18,21], dam failure [22–24] and bubble rising [25,26]. However, the results of the
35
36 Gibou et al. [27] showed that, although LS model can accurately compute the geometrical
37
38 quantities of the interface (i.e. interface normal and curvature) using a smooth implicit Heaviside
39
40 function, this model is typically plagued by mass conservation issues which in turn leads to a
41
42 substantial loss of accuracy. On the other hand, Yin et al. [28] and Marić et al. [29] conducted
43
44 comprehensive reviews on the last application of the Volume-Of-Fluid model and concluded
45
46 that, although VOF model can intrinsically guarantee discrete mass conservation and is relatively
47
48 simple to implement in practice, this model is characterized by some crucial drawbacks such as:
49
50
51
52
53
54
55
56
57
58
59
60
61
62
63
64
65

1
2
3
4 (1) unphysical growth of interface thickness arising from false-diffusion errors [30,31], (2)
5
6 inaccuracy in estimating interface curvature [32,33], (3) unphysical pressure/velocity
7
8 fluctuations around the material discontinuity [34,35] which can immensely jeopardize the
9
10 reliability and consistency of the numerical solutions and render nonphysical flow physics,
11
12 accordingly. During last decades, substantial research efforts have been devoted to address the
13
14
15
16
17
18
19
20
21
22
23
24
25
26
27
28
29
30
31
32
33
34
35
36
37
38
39
40
41
42
43
44
45
46
47
48
49
50
51
52
53
54
55
56
57
58
59
60
61
62
63
64
65

Inspired by work of Boris and Book [36], in a pioneering works, Harten [37] and Leonard [38] introduced the notion of High resolution non-oscillatory differencing schemes to address the problem of interface smearing and suppress detrimental effects of numerical diffusion. They proposed two novel second-order bounded convection schemes so-called TVNI and SHARP based on the TVD (Total Variation Diminishing) [39] and NVD (Normalized Variable Diagram), and found that, monotone difference schemes can offer better iterative convergence properties in comparison with the classical unbounded oscillatory ones such as second-order Upwind (LUD), Central Differencing (CD), QUICK and Fromm [40], when applied to the implicit solution methods. Moreover, they pointed out that, the implementation of the hybrid non-linear flux-limiter schemes exhibit better resolution of steep gradients and discontinuities but at the expense of a higher computational cost due to the switching between different flux-limiter schemes especially when the interface orientation is tangential to the flow direction. Similar findings were also reported by Zhang et al. [31] who conducted a comprehensive literature survey on the various TVD schemes and highlighted that gradually-switching smooth flux-limiters can lead to the better convergence behavior compared to the piecewise linear limiter functions. From then on, various conservative differencing schemes were constructed by using the unique relationship between NVD and TVD constraints. Examples include SOUCUP [41],

1
2
3
4 MINMOD [37], SMART [42], TOPUS [43], HLLP [44], GAMMA [45], Van Leer [46],
5
6 SMARTER and LPPA [30]. However, the results of Ubbink et al. [47] revealed that, the global
7
8 order of these schemes are restricted to the second-order in any case. In addition to that, they are
9
10 derived based on one-dimensional assumption which can hinder their further applications in
11
12 multi-dimensional problems. To overcome this issue, they proposed a blended control-volume
13
14 flux-limiter formulation named as “CICSAM” based on the Normalised Variable Diagram which
15
16 switches smoothly between two high resolution schemes namely Hyper-C and Ultimate-Quickest
17
18 (UQ). They claimed that, CICSAM is capable of preserving the integrity of the interface while
19
20 reducing the diffusion errors. However, in the same context, Malgarinos et al. [48], Nguyen et al.
21
22 [49], Waławczyk et al. [50] questioned the capability of CICSAM scheme in handling large
23
24 topological changes and stressed that the CICSAM scheme cannot satisfactory recover interface
25
26 sharpness and is also prone to numerical smearing due to its inherent low order of accuracy. In
27
28 order to mitigate the adverse effects of numerical diffusion and to cope with heterogeneity in
29
30 physical properties, Garoosi et al. [51] proposed a novel third-order accurate flux-limiter
31
32 function which guarantees boundedness condition while maintaining interface shape. They
33
34 evaluated and tested the feasibility and accuracy of their scheme against a set of canonical test
35
36 cases and showed that, the newly developed TVD function can successfully meet the
37
38 completeness requirements for convective stability, convergence criteria, monotonicity and
39
40 algorithmic simplicity. However, further assessment of performance and outcome is required
41
42 prior to implementing/extending it to some intricate multi-fluid problems.
43
44
45
46
47
48
49
50
51
52

53 Referring to the second drawback related to the VOF model, Pozzetti et al. [52], Dianat et al.
54
55 [53] and Zhang et al. [54] suggested the use of PIMPLE algorithm (PISO-SIMPLE algorithm
56
57 available in OpenFOAM® platform) to circumvent the problem of velocity/pressure jump across
58
59
60
61

1
2
3
4 the interface. However, since an additional iterative SIMPLE algorithm is incorporated into the
5
6 standard PISO loop, this pressure-based solver seems not to be computationally efficient
7
8 particularly when it will be extended to the three-dimensional real-life problems with large scale
9
10 [55]. To remedy this deficiency, Garoosi et al. [51] proposed a novel hybrid semi-iterative
11
12 PISOC algorithm by the combination of the classical PISO [56] and Two-step projection [57]
13
14 models. Their results showed that, PISOC algorithm can appreciably remove the spurious
15
16 pressure/velocity oscillations from fluid domain with affordable computational cost.
17
18
19
20
21

22 Finally, as stated before, the third challenge faced by VOF model is to determine the exact value
23
24 of interface normal/curvature for the accurate enforcement of surface tension force. To tackle
25
26 this problem, Youngs [58,59] introduced the first-order accurate interface reconstruction
27
28 technique in the context of the PLIC concept and then successfully utilized for modelling of
29
30 Rayleigh-Taylor Instability problem. However, despite its many uses and applications in both
31
32 commercial and open source CFD softwares, the analytical investigation of Pilliod et al. [33]
33
34 revealed that, Youngs' method cannot exactly reproduce all linear interface and is prone to
35
36 fragment a smooth front. As an alternative approach, he proposed the ELVIRA technique for the
37
38 reconstruction of interface and demonstrated that the method is second-order accurate on smooth
39
40 interfaces. This technique was then coded and adopted by Garoosi et al. [51] for numerical
41
42 investigation of multiphase flows with moving interfaces.
43
44
45
46
47
48
49

50 The above literature review clearly demonstrate that, the previous work of Garoosi et al. [51]
51
52 systematically addressed three crucial shortcomings related to the interface-capturing VOF
53
54 model. However, these improvements still need further verifications before being generalized to
55
56 multi-fluid flows with high density contrast and surfactant. Based on the above explanation, the
57
58 purpose of the present work is twofold: (1) to demonstrate the versatility of the enhanced VOF
59
60
61

1
2
3
4 model in handling two- and three-phase flows, and (2) to introduce two novel benchmark
5
6 problems for CFD validation. To accomplished this objectives, in the first stage of the current
7
8 work, the validity and accuracy of the enhanced VOF model is further tested against the
9
10 additional canonical test cases including draining of liquids from the storage tank (tank draining),
11
12 single rising bubble, three-phase Rayleigh-Taylor Instability and dam-break flows over dry and
13
14 wet beds. In the second stage, the verified VOF model will be employed to investigate two new
15
16 challenging cases namely: merging of two rising bubbles with different densities and diameters,
17
18 aiming to provide the state-of-the-art benchmark solutions and up-to-date data set for CFD
19
20 validations. To the best of authors' knowledge, such challenging benchmark problems have not
21
22 been reported in the literature. The simulated results are presented in forms of volume fraction
23
24 and pressure contours and related interface profile.
25
26
27
28
29
30

31 32 **2. Problem statement and governing equations**

33
34
35 The geometrical configurations of physical models with associated boundary conditions are
36
37 portrayed in Fig. 1. In the present work, the first six canonical problems (cases 1-6) are chosen to
38
39 further verify the capability and versatility of the improved version of VOF model in dealing
40
41 with the multi-fluid flow problems with low and high density contrasts whereas cases 7 and 8 as
42
43 two new benchmark problems will be analyzed in details. The numerical analyses were carried
44
45 out using FORTRAN 90 programming language where the Intel® Visual FORTRAN Compiler
46
47 19.0 was used for the compilation of the developed code. The governing equations (i.e. mass,
48
49 momentum and volume fraction) for the Newtonian, laminar and incompressible multiphase
50
51 flows in the Eulerian description can be written as follows [47,60]:
52
53
54
55
56
57

$$58 \quad \frac{\partial \rho}{\partial t} + \frac{\partial \rho u}{\partial x} + \frac{\partial \rho v}{\partial y} = 0, \quad (1)$$

59
60
61

$$\frac{\partial \rho_m u}{\partial t} + \frac{\partial \rho_m uu}{\partial x} + \frac{\partial \rho_m vu}{\partial y} = -\frac{\partial p}{\partial x} + \left[\frac{\partial}{\partial x} \mu_m \left(\frac{\partial u}{\partial x} \right) + \frac{\partial}{\partial y} \mu_m \left(\frac{\partial u}{\partial y} \right) \right] + F_{ST} \quad (2)$$

$$\frac{\partial \rho_m v}{\partial t} + \frac{\partial \rho_m uv}{\partial x} + \frac{\partial \rho_m vv}{\partial y} = -\frac{\partial p}{\partial y} + \left[\frac{\partial}{\partial x} \mu_m \left(\frac{\partial v}{\partial x} \right) + \frac{\partial}{\partial y} \mu_m \left(\frac{\partial v}{\partial y} \right) \right] + \rho_m g + F_{ST} \quad (3)$$

$$\frac{\partial \varphi}{\partial t} + \frac{\partial \varphi u}{\partial x} + \frac{\partial \varphi v}{\partial y} + \nabla \cdot (\varphi (1-\varphi) \mathbf{u}_R) = 0 \quad (4)$$

$$\frac{\partial \lambda}{\partial t} + \frac{\partial \lambda u}{\partial x} + \frac{\partial \lambda v}{\partial y} + \nabla \cdot (\lambda (1-\lambda) \mathbf{u}_R) = 0 \quad (5)$$

$$\varphi + \lambda = 1 \text{ or } \varphi + \lambda + \gamma = 1 \quad (6)$$

where u , v , g , p and t denote the velocity components in 2D Cartesian coordinate system, gravity acceleration, pressure and time, respectively. ρ_m and μ_m are density and dynamic viscosity of the mixture which can be calculated through the φ -, λ - and γ -weighted average of phases in each computational cell as [61]:

$$\rho_m = \varphi \rho_1 + (1-\varphi) \rho_2 \quad (7)$$

$$\mu_m = \varphi \mu_1 + (1-\varphi) \mu_2 \quad (8)$$

$$\rho_m = \varphi \rho_1 + \lambda \rho_2 + (1-\lambda-\varphi) \rho_3 \quad (9)$$

$$\mu_m = \varphi \mu_1 + \lambda \mu_2 + (1-\lambda-\varphi) \mu_3 \quad (10)$$

In the above formulations, Eqs. (7)-(8) are adopted for the approximation of the density and viscosity of two-fluid flow problems whereas Eqs. (9) and (10) are used to predict the fluid properties in the three-phase problems with subscripts 1, 2 and 3 being reference fluid-components. The last term F_{ST} in Eqs. (2) and (3) stands for the surface tension force which is approximated based on the Continuum Surface Force (CSF) model proposed by Brackbill et al. [62] as:

$$F_{ST} = \sigma k \nabla \varphi \quad (11)$$

where σ denotes the surface tension coefficient between two phases and k represents the curvature of interface defined as [28]:

$$k = -\nabla \cdot \mathbf{n} = -\nabla \cdot \left(\frac{\nabla \varphi}{|\nabla \varphi|} \right) \quad (12)$$

$$\mathbf{n} = \frac{\vec{n}}{|\vec{n}|}, \vec{n} = \nabla \varphi \quad (13)$$

where \mathbf{n} indicates the interface unit normal vector which is pointing away from the interface. The third terms ($\nabla \cdot (\varphi(1-\varphi)\mathbf{u}_R$) and $\nabla \cdot (\lambda(1-\lambda)\mathbf{u}_R)$) in the transport equations (i.e. Eqs. (4) and (5)) are known as the Artificial Compression Term (ACT) [63–65] which are non-zero in the close proximity of interface region owing to the existence of $\varphi(1-\varphi)$ and $\lambda(1-\lambda)$ terms. Note that, the additional ACT term has a tendency to preserve the interface sharpness especially when the flow is tangential to the interface. \mathbf{u}_R is the compressive velocity which act perpendicular to the fluid interface and may be estimated based on maximum velocity magnitude as follows [66,67]:

$$\mathbf{u}_R = C_\varphi |\vec{u}| \mathbf{n} = C_\varphi |\vec{u}| \frac{\nabla \varphi}{|\nabla \varphi|} \quad (14)$$

The coefficient $C_\varphi = 0.5$ is the compression factor which controls the strength of interface compression and ranges from 1 to 2 dependent on the grid resolution [68–70].

3. Numerical methodology

The system of governing partial differential equations (Eqs. 1-5) are solved using finite volume method (FVM) on a staggered grid arrangement where no interpolation is required to estimate velocity components at the scalar cell faces which in turn results in the proper velocity-pressure coupling and total elimination of unphysical checkerboard pressure fluctuations [71]. Structured

1
2
3
4 uniform mesh in X and Y -directions are utilized for all computations and the transient terms in
5
6 the momentum and transport equations are treated implicitly using a second-order backward
7
8 differencing scheme [72]. The diffusion terms in the Navier-Stokes equation is approximated by
9
10 the second-order central differencing scheme while a third-order TVD upwinding scheme
11
12 proposed by Garoosi et al. [51] is utilized for the discretisation of the convection terms in
13
14 momentum and volume fraction equations. In order to enforce the conservation of mass in
15
16 unsteady incompressible multiphase flows, the semi-iterative version of the improved PISO
17
18 algorithm is applied for the treatment of the pressure-velocity coupling where two classical PISO
19
20 [56] and Two-step projection (Chorin's model [57]) approaches are merged in the single hybrid
21
22 algorithm (labelled hereafter as PISOC). Details regarding the solution procedure and derivation
23
24 of the PISOC algorithm can be found in previous work of Garoosi et al. [51] (see also Appendix
25
26 A) . To further enhance the stability and consistency of the numerical solutions, the second-order
27
28 interface reconstruction technique (ELVIRA) pioneered by Pilliod et al. [33] is implemented for
29
30 the estimation of the interface curvature and the enforcement of the surface tension force,
31
32 accordingly.
33
34
35
36
37
38
39
40

41 **4. Validation and verification**

42
43
44 To verify the feasibility and robustness of the proposed VOF model in handling multiphase flows
45
46 with sever interface deformation and fragmentation, six different challenging benchmark test
47
48 cases are numerically reproduced in this section. The first, second and third canonical test cases
49
50 are classical dam-break flows (cases 1 and 2) and tank draining (case 3) where owing to sudden
51
52 collapse of liquid column and high density contrast between phases (water-air fluids), the
53
54 hydrodynamic/hydraulic behavior of the free-surface flow is characterized by series of interface
55
56 rupture and coalescence events. The fourth and fifth benchmark examples are three-phase
57
58
59
60
61

1
2
3
4 Rayleigh-Taylor Instability problems (case 4 and 5) where due to the low density ratio between
5
6 phases and the appearance of Kelvin-Helmholtz instability within the computational domain, the
7
8 fluid interface is likely to undergo sever distortion including twisting, flattening or even
9
10 filamentation. The last benchmark problem (case 6) involves the study of classical bubble rising
11
12 with high density and viscosity ratios where due to the existence of the surface tension force and
13
14 development of the wake region, the phenomenon so-called bubble detachment with associated
15
16 interface filamentation are likely to occur within the fluid domain. The obtained results are
17
18 presented in separate subsections and discussed in details.
19
20
21
22
23

24 **4.1.Dam-break flow over dry and wet beds (cases 1 & 2)**

25
26
27 Transient evolution and hydrodynamic characteristics of dam-break flow over a horizontal dry
28
29 and wet bed are analyzed in this subsection. As sketched in Fig. 1, the calculations in the first
30
31 benchmark problem (case 1) are carried out in a prismatic rectangular flume with dimensional
32
33 size of $D=1.4m$ and $L=1.61m$ where the water column ($g=9.81ms^{-2}$, $\rho=997kgm^{-3}$,
34
35 $\mu=855\times 10^{-6}kgm^{-1}s^{-1}$) with initial width and depth of $W=H=0.6m$ is stored on the left side
36
37 of the reservoir. The rest of the enclosure is occupied by air (
38
39 $\rho=1.0kgm^{-3}$, $\mu=184\times 10^{-7}kgm^{-1}s^{-1}$) as a secondary phase and the effects of surface tension
40
41 force ($\sigma=0.071Kgs^{-2}$) are taken into consideration. The simulation is performed on the
42
43 uniform grid resolution of 500×435 (in x - and y -directions) and the initial zero values are
44
45 assigned for pressure and velocity across the whole channel ($p=0, u=v=0ms^{-1}$). The time
46
47 histories of the water level height are monitored at three different sites ($l_1=0.3m, l_2=1.114m$
48
49 and $l_3=1.362m$) and pressure variations are recorded by two sensors installed on the
50
51
52
53
54
55
56
57
58
59
60
61

1
2
3
4 downstream wall ($h_{R1} = 0.03m$ and $h_{R2} = 0.08m$). No-slip impermeable wall boundary conditions
5
6
7 are imposed on all stationary walls and obtained results in terms of volume fraction and pressure
8
9 contours are displayed in Fig. 2. The predicted results reveal that once the virtual lifting gate is
10
11 removed, the standing water column descends downward under the gravity force and is promptly
12
13 replaced by traveling wave, indicating the rapid conversion of the potential energy of the system
14
15 into the kinetic one. As time progresses ($0 < T < 1.61$), the flooding wave freely propagates over
16
17 the initially dry bed and elongates horizontally until it encounters the boundary layer of
18
19 downstream wall approximately at time $T = 1.61$ where the first impact pressure and wave
20
21 deflection occur ($P_{\max 1, R1} = 2.29$, $P_{\max 1, R2} = 1.44$). However, since the right wall is rigid and
22
23 impermeable, the resultant impact wave starts to deviate upward and moves vertically along the
24
25 rigid wall, leading to the formation of the ascending jet in that area. It is worth mentioning that,
26
27 this stage is also accompanied by the emergence of semi-hydrostatic pressure distribution and
28
29 stagnation point (or fluid trapping phenomenon) on the bottom-right corner of the flume which
30
31 manifest themselves through an asymptotic reduction in the values of pressure load during the
32
33 time period of $1.61 \leq T \leq 4.15$ (see also Fig. 3). As time proceeds, the intense upwelling jet
34
35 grows in size and amplitude until the tip of the liquid jet reaches its maximum elevation at
36
37 $Y = y/H \approx 2.0$ and $T = 3.2$ which is approximately twice the initial water level height at dam
38
39 site. Similar finding was observed and documented by Colagrossi et al. [73] who numerically
40
41 investigated the same benchmark problem but with different initial water depth. Later, due to
42
43 restoring action of the gravity force, the up-rushing liquid jet is eventually flipped down and
44
45 decelerated, leading to the creation of reverse plunging wave breaker with maximum wave crest
46
47 height of $Y = y/H \approx 0.97$ which is nearly equals to the initial water level height at upstream
48
49 region (compare two snapshots of the volume fraction contours at time instants of $T = 0.638$ and
50
51
52
53
54
55
56
57
58
59
60
61

1
2
3
4 $T = 4.707$). In addition, a close inspection of the pressure contours in Fig. 2 illustrates that
5
6 during this period of evolution, the quasi-hydrostatic pressure zone expands to occupy larger part
7
8 of the rolling wave which indicates that the main flow is primarily governed by transverse inertia
9
10 force in x -direction. This phenomenon corresponds to the progressive augmentation in time
11
12 histories of pressure variations during the period of $4.15 < T \leq 5.05$ (see also Fig. 3). Ultimately,
13
14 the backward plunging breaker collapses obliquely onto the advancing water surface below and
15
16 penetrates it, producing an egg-shaped air cushion structure and the second peak pressure (
17
18 $P_{\max 2,R1} = 1.18, P_{\max 2,R2} = 1.09$) at $T = 5.05$. The position of shock pressure is also visible around
19
20 the collapse site (see snapshot of the pressure contours at $T = 5.026$) which presumable results
21
22 from the immersion of reflected jet. However, as mentioned before, the impact of the plunging
23
24 wave on the wetted bed generates a new surge with moderate celerity which spurts from the free-
25
26 surface of incoming dam-break wave and travels obliquely towards the upstream area, resulting
27
28 in a strong air-water flow interaction with associated gas entrapment.
29
30
31
32
33
34
35
36

37 Comparison of the obtained results with experimental and numerical data of Lobovský et al. [74]
38
39 and Sun et al. [75] are plotted in Fig. 3. The overall examination of the figure shows that, the
40
41 snapshots of the free-surface profile at three different time instants together with the non-
42
43 dimensional pressure variations predicted from the current work are in a satisfactory agreement
44
45 with previously published data. Moreover, it is evident that the proposed model can effectively
46
47 preserve the integrity and sharpness of the interface especially during the occurrence of the
48
49 plunging breaker when flow-to-grid skewness is substantial. Thanks to the hybrid PISOC
50
51 algorithm, the pressure field is totally free from the spurious fluctuations, which in turn confirms
52
53 superiority of the proposed semi-iterative pressure-based model over the classical PISO and
54
55 Two-step projection (Chorin's model) approaches in dealing with the highly non-linear
56
57
58
59
60
61

1
2
3
4 incompressible fluid flows. Finally, it is worthwhile to mention that, the time histories of non-
5
6 dimensional surge front location (X_{front}) and water column height at three different sections are
7
8 presented in Fig. 3 as additional information which have not been reported in the literature.
9

10
11
12 The problem of dam break flow over the initially wet bed is considered and reproduced here as a
13
14 second test case (case 2). This small-scale laboratory experiment was originally conducted by
15
16 Jánosi et al. [76] and then numerically reproduced by Jonsson et al. [77], Ye et al. [78], Crespo et
17
18 al. [79] and Gu et al. [80]. The configuration of the prototype experiment is sketched in Fig. 1.
19

20
21 As it can be observed, the simulation is carried out in a prismatic rectangular duct with
22
23 dimensional size of $D = 0.3m$ and $L = 1.2m$ where the rectangular water column ($g = 9.81ms^{-2}$,
24
25 $\rho = 997kgm^{-3}$, $\mu = 855 \times 10^{-6}kg m^{-1}s^{-1}$) with width and depth of $W = 0.38m$ and $H = 0.15m$ is
26
27 connected to the downstream wet bed with initial water level height of $B = 0.018m$. The rest of
28
29 the channel is filled by air ($\rho = 1kgm^{-3}$, $\mu = 184 \times 10^{-7}kg m^{-1}s^{-1}$) as a secondary phase and the
30
31 effects of surface tension force ($\sigma = 0.071Kgs^{-2}$) are taken into account. The simulation is
32
33 performed on the uniform grid resolution of 480×120 (in x - and y -directions) and the initial zero
34
35 values are assigned for pressure and velocity fields ($p = 0, u = v = 0ms^{-1}$). The time variations of
36
37 the free-surface profile are recorded at three different sections ($l_1 = 0.1m, l_2 = 0.5m$ and $l_3 = 0.9m$
38
39) and dynamic pressure variations on the bottom wall are monitored by three virtual sensors
40
41 deployed at $l_1 = 0.1m, l_2 = 0.7m$ and $l_3 = 1.0m$. No-slip impermeable wall boundary conditions
42
43 are imposed on all rigid walls and predicted results in forms of volume fraction and pressure
44
45 fields are portrayed in Figs. 4 and 5. Generally, although the global hydrodynamic and
46
47 morphologic behavior of dam failure processes over the dry and wet beds are relatively identical,
48
49 there are substantial differences when they come to hydraulic jump and plunging jet formations
50
51
52
53
54
55
56
57
58
59
60
61

1
2
3
4 [81]. It is evident from Fig. 4 that, contrary to the previous benchmark problem, owing to the
5
6 head water differences between the falling water and downstream wet deck, the shock wave in
7
8 form of weak ascending jet is immediately appeared at the junction of the upstream and the
9
10 downstream areas and projected obliquely over the underlying wet bed as its kinetic energy
11
12 increases. As time goes on, the front face of the stress wave steepens and becomes gradually
13
14 horizontal. In these circumstances, due to the influence of the gravity force, the vertical celerity
15
16 of the advancing wave decreases and consequently the resultant plunging breaking jet starts to
17
18 fall down and hits the undisturbed water surface at $T=2.205$ and $x \approx 0.69m$, leading to the
19
20 emergence of the entrapped cavity (air tube) with a visibly large radius of curvature. This
21
22 phenomenon corresponds to the rapid augmentation in the pressure time history ($P_{\max 1,l_2} = 0.326$)
23
24 recorded by sensor 2 installed at $l_2 = 0.7m$ (see also Fig. 5). However, the remaining portion of
25
26 the kinetic energy of the system causes the overturning jet to rebound from the wet bed as a new
27
28 ascending wave and travels downstream. As expected, this mechanism results in the creation of
29
30 the second large air-cushion structure at $T=3.52$ and $x \approx 0.985m$ with pronounced
31
32 concentrations of vorticity. A third plunging action can also be observed during the time
33
34 period of $3.528 \leq T \leq 4.491$ but at a much smaller scale. The comparison of the obtained results
35
36 with previous works of Jánosi et al. [76] and Gu et al. [80] in Fig. 5 shows that, there is an
37
38 excellent agreement between outcomes of the current study and published experimental data.
39
40 However, as anticipated, it is evident that, the conventional VOF-LS model fails to predict the
41
42 main features of the process which can be attributed to two aforementioned shortcomings
43
44 associated with interface-capturing methods. On the other hand, the zoomed-in views of the
45
46 interface in Fig. 5 reveal that, the proposed VOF model successfully alleviates the detrimental
47
48 effects of numerical diffusion, thereby preserving the sharpness of the interface. Thanks to the
49
50
51
52
53
54
55
56
57
58
59
60
61
62
63
64
65

1
2
3
4 proposed TVD convection scheme, the thickness of the interface is efficiently controlled and
5
6 limited to the 2-3 grid spacing and morphological changes of the dynamic process are well
7
8 reproduced. Finally, similar to the previous test case, the time histories of the water level height
9
10 and pressure variations at three different sections/points are presented in Fig. 5 which have not
11
12 been reported in published literature.
13
14

15 16 17 **4.2. Tank draining problem (case 3)** 18

19
20 The temporal evolution and hydraulic characteristics of liquid draining from a vessel is examined
21
22 in this subsection. The initial configuration of the system is similar to numerical work of
23
24 Ghadampour et al. [82] where a quiescent column of water ($g = 9.81ms^{-2}$, $\rho = 997kgm^{-3}$,
25
26 $\mu = 855 \times 10^{-6}kg m^{-1}s^{-1}$) with width and height of $W = H = 0.15m$ is initially confined in the left
27
28 side of the square reservoir with physical dimension of $L = D = 0.35m$. Similar to the previous
29
30 test case, the rest of the reservoir is filled with air ($\rho = 1kgm^{-3}$, $\mu = 184 \times 10^{-7}kg m^{-1}s^{-1}$) and the
31
32 effects of the surface tension force ($\sigma = 0.071 Kgs^{-2}$) are taken into account. The simulation is
33
34 performed on uniform grid size of $\Delta x = \Delta y = 0.001m$ (352×352 mesh resolution) and no-slip
35
36 boundary condition of zero velocity is imposed on all rigid walls. In order to induce the
37
38 discharging process of water storage tank (partial breach dam-break flow), the stationary rigid
39
40 wall and drain port with dimensions of $R = 0.58L = 0.203m$ and $S = 0.1L = 0.035m$ are installed
41
42 at a distance of $x = 0.15m$ from the upstream boundary wall. Qualitatively, topological
43
44 characteristics and hydrodynamic peculiarities of the tank draining are analogous to the former
45
46 benchmark problem where conversion of potential energy into kinetic one occurs immediately
47
48 once the sluice gate is opened. It is evident from Fig. 6 that, after the removal of the submerged
49
50 gate, the stored water starts flowing through the breach and progressively spread over the flume
51
52
53
54
55
56
57
58
59
60
61

1
2
3
4 bed until the flood wave impacts the opposite wall. During this process, the water level height at
5
6 the storage site gradually decreases which implies that the fluid flow in upstream of a vertical
7
8 sluice gate is subcritical. On the other hand, the appearance of a hydraulic jump at
9
10 $0.485 \leq T \leq 1.536$ conveys that the fluid flow in the downstream is supercritical and the
11
12 discharge may be determined by the upstream water depth and the gate opening [83]. However,
13
14 after the impingement of the wave front onto the right wall, the surge wave changes its direction
15
16 and propagates vertically until the wave crest reaches the its maximum position ($Y = y/H \approx 2.0$)
17
18 at $T \approx 3.153$. As anticipated, this mechanism leads to the development of the pressure shock
19
20 region ($P_{\max 1} = 1.67 m$) on the bottom-right corner of the enclosure at $T = 1.21$ which is
21
22 monitored by sensors 1 deployed on the right wall ($h_{R1} = 0.0 m$, see also Fig. 7). As time goes
23
24 on, due to the retarding effects of gravity force, the newly generated sharp-crested wave (jet-like
25
26 structure) starts to evolve into the plunging breaker which ultimately hits and immerses into the
27
28 oncoming water discharge, leading to the establishment of an egg-shaped air cushion structure
29
30 and second impact pressure ($P_{\max, R1} = 1.420$, $P_{\max, R2} = 1.056$ and $P_{\max, R3} = 0.491$) at $T = 4.528$.
31
32
33
34
35
36
37
38
39 From the spatial anatomy of the stress wave at $T = 4.528$ one can deduce that, due to the
40
41 backward movement of the impinging jet and forward momentum of the water discharge, a
42
43 clockwise rotating eddy may be developed within the air pocket. This flow pattern was originally
44
45 termed "*plunging vortex*" by Basco [84] in the context of wave breaking. Another key feature of
46
47 this interaction is the axial meeting of these two water masses which leads to the strong impulse
48
49 wave and large pressure gradients on the flume floor at $x = 0.24 m$ (see pressure contour at
50
51 $T = 4.528$). Note that, from the hydraulics point of the view, the impingement zone of a
52
53 plunging jet is referred to as the *submerged hydraulic jump* region where mechanic energy
54
55 (kinetic energy) of the slanting jet is irreversibly dissipated into the pressure shock [85].
56
57
58
59
60
61

1
2
3
4 Nevertheless, the residual or small excess momentum of the system with the aid of advancing
5 plunging vortex cause the submerged jet to rebound from the underlying wetted bed and migrates
6
7 towards the sluice gate where due to the integrated interaction of pseudo-plunging breaker and
8
9 rigid gate, the third impact pressure and second air entrapment (air cavity structure) take place.
10
11
12

13
14
15 Qualitative comparison of the obtained results with numerical work of Ghadampour et al. [82] in
16
17 Fig. 7 shows that, the early stage of the tank draining process is well predicted by the enhanced
18
19 VOF model. As can be seen from the results, the thickness and sharpness of the interface are
20
21 well controlled and preserved during the simulation which vividly proves the capability of the
22
23 proposed modifications in capturing steep gradients and retaining the boundedness of the volume
24
25 fraction between $0 \leq \varphi \leq 1$. Furthermore, it is evident that, the pressure field is satisfactory
26
27 smoothed and the propagation of numerical diffusion arising from flow-to-grid skewness is
28
29 effectively attenuated by the proposed third-order bounded TVD convection scheme. However,
30
31 due to lack of essential information concerning tank draining problem in Ref [82], the pressure
32
33 time history at three different marked points on the right (h_{Ri}) and left (h_{Li}) walls of the
34
35 enclosure together with the time histories of wave front location (X_{front}) and water level heights
36
37 at two different sections ($l_1 = 0.06m$ and $l_2 = 0.26m$) are provided as supplementary data on
38
39 present problem which may be utilized by scholars for assessment and validation of various CFD
40
41 tools. However, before ending this section, it should be noted that, the small peak in the time
42
43 histories of pressure variations recorded by sensors $h_{L1} = 0.0m$, $h_{L2} = 0.05m$ $h_{L3} = 0.1m$ on the
44
45 left wall can be attributed to the assigning initial zero pressure instead of imposing pre-known
46
47 hydrostatic pressure value ($P_{Initial} = \rho gH$). This statement implies that, the pressure field is
48
49 progressively determined through the PISOC algorithm during the simulation.
50
51
52
53
54
55
56
57
58
59
60
61

4.3. Three-phase Rayleigh-Taylor Instability (cases 4 and 5)

The initial growth and tortuous evolution of three-phase Rayleigh-Taylor Instability problem is investigated in this subsection. The benchmark test cases were originally introduced by Garoosi et al. [86] in the context of the Lagrangian description by means of the Moving Particle Semi-implicit (MPS) method. As sketched in Fig. 1, three immiscible incompressible viscous fluids with nominal densities of $\rho_H = 4.0$, $\rho_M = 2.0$ and $\rho_L = 1.0$ are sequentially positioned at the top, middle, and bottom parts of the enclosure, respectively. All fluids have identical kinematic viscosities ($\nu_H = \nu_M = \nu_L = 0.01$). The simulations are conducted in the computational domain with size of $[0, H] \times [0, 3H]$ where $H = 1m$ denotes the width of the enclosure. The initial positions of interfaces between each pair of the fluids in configuration of case 4 are set to $y_1 = 1.0 + 0.1 \times \cos(2\pi x)$ and $y_2 = 2.0 + 0.1 \times \cos(2\pi x)$ whereas the interfaces in case 5 are initialized as $y_1 = 1.0 + 0.1 \times \cos(2\pi x)$ and $y_2 = 2.0 - 0.1 \times \cos(2\pi x)$, respectively. The instability in both cases is governed by non-dimensional Reynolds and Atwood numbers equal to $Re = \rho_H H \sqrt{gH} / \mu_H = 420$ and $At = (\rho_H - \rho_L) / (\rho_H + \rho_L) = 3/5$, respectively. The mesh resolution of 300×900 is chosen for both cases and the effects of surface tension force are neglected. However, contrary to the previous test case, since three distinct fluids are engaged in cases 4 and 5, Eqs. (4) and (5) are utilized to calculate the volume fractions of dense (φ) and middle (λ) fluids, respectively while the formula ($\varphi + \lambda + \gamma = 1$) in Eq. (6) is employed to estimate the volume fraction of the lighter fluid. Figs. 8 and 9 exhibit the time evolution of the density contours in cases 4 and 5. As displayed in Fig. 8, in the early stages of the RTI development, the heavy fluid (ρ_H) on top in case 4 starts to penetrate into the less-dense phase (ρ_M), meanwhile the middle fluid rises up from the sides of the enclosure in the form of plume-

1
2
3
4 like structure. However, since both interfaces in case 4 are perturbed in the same directions, this
5
6 course of the event also occurs between middle (ρ_M) and lighter (ρ_L) fluids. Hence, two pairs
7
8 of bubble-spike structures with associated vortex sheets are established within the enclosure.
9
10 Scrutiny of the figure illustrates that, during the early stages of the evolution ($0 \leq T \leq 1.575$), the
11
12 harmonic growth of the fluid interfaces remains symmetrical with respect to the center of the
13
14 enclosure which indicates that the instability still follows the linear theory [87]. However, as
15
16 expected after a finite time, due to the low density disparity between phases, the main flow
17
18 becomes unstable to the Kelvin-Helmholtz shear instability which causes the initial disturbance
19
20 to lose its symmetry feature and enter the weakly nonlinear mode ($1.575 < T \leq 2.520$) [88]. As
21
22 time goes on, the formation of the spikes gets more prominent and intensity of the Kelvin's
23
24 circulation increases. This intermediate stage of the development ($2.520 < T \leq 3.150$) is also
25
26 accompanied by the broadening of vortex shedding in the wake of spike which manifest itself
27
28 through inward folding of the interface. As the instability grows further ($3.150 < T \leq 4.095$), the
29
30 rising wings of the lighter fluid start to embrace the falling spike of the denser fluid, resulting in
31
32 the appearance of the tulip-shaped structure (or harpoon-like pattern). In this circumstance, the
33
34 tails of the roll-ups evolve into the complicated pattern and consequently the fluid flow enters the
35
36 fully non-linear regime where the corresponding contraction of the dense fluid alters the pattern
37
38 into the needle-shaped spike. The surrounded spike keeps moving downward until it reaches the
39
40 boundary layer of the bottom wall, giving rise to the substantial and sharp distortion of the
41
42 interface with pronounced concentrations of vorticity. Inspection of the results in Fig. 8 also
43
44 reveals that, the total displacement of the advanced bubble (lighter fluid) is considerably lower
45
46 than that of the falling fluid. This finding may be attributed to the existence of some secondary
47
48 eddies near the tips of the needle-shaped spike and due to the long horizontal distance between
49
50
51
52
53
54
55
56
57
58
59
60
61

1
2
3
4 the primary spike and vertical walls of the container where no-slip velocity boundary condition is
5
6 imposed.
7
8
9

10 However, Fig. 9 illustrates that by altering the direction of the upper cosinusoidal perturbation
11
12 from $y_2 = 2.0 + 0.1 \times \cos(2\pi x)$ to $y_2 = 2.0 - 0.1 \times \cos(2\pi x)$, a different scenario appears within
13
14 the container. It is evident that, since the interfaces in case 5 are disturbed in the opposite
15
16 directions, at the early stages of the evolution ($0 \leq T \leq 2.520$), the middle fluid starts to penetrate
17
18 simultaneously into the adjacent heavy and lighter fluids whereas the edges of the disturbed
19
20 interfaces move radially towards the central zone of the enclosure to fulfill the need for the mass
21
22 conservation. As the current progresses further ($2.520 < T \leq 3.570$), the flow resistance of the
23
24 lighter and denser fluids becomes important which causes the sides of the medium phase to roll-
25
26 up and amalgamate into the unsteady swirling flow (vortex shedding). As stated before, this flow
27
28 pattern is commonly cited as the onset of the Kelvin-Helmholtz Instability (KHI), which denotes
29
30 the presence of the shear force in the rear of the spikes. As the simulation time proceeds (
31
32 $3.570 < T \leq 5.250$), the motion of the tips of a spikes slows down and interfaces undergo
33
34 significant deformation. It can be seen from Fig. 9 that, during this process, the rising sheet
35
36 plumes (lighter fluid, ρ_L) start to bifurcate and cover the falling dense fluid (ρ_H), forming a
37
38 heart-like structure within the enclosure. In fact, the creation of the heart-like structure (Pitchfork
39
40 bifurcation phenomenon [89]) and its expansion/broadening in the x -direction at the central
41
42 portion of the fluid domain, are the signs of the fluid entrapment phenomenon and development
43
44 of the quasi stagnation point which causes the falling liquid to get stuck in that region.
45
46
47
48
49
50
51
52
53
54
55

56 Qualitative and quantitative comparison in Fig. 10 demonstrate excellent agreement between the
57
58 results of the present Eulerian VOF model with the data of Lagrangian MPS simulations [86].
59
60
61

1
2
3
4 More precisely, it is evident that, the bubble-spike structures in both cases alongside the
5 maximum and minimum positions of the dense and lighter fluids are satisfactory reproduced and
6 predicted using the enhanced VOF method. However, the small differences between two results
7 can be attributed to the nature of the two models to address the problem of physical
8 discontinuities in the multiphase flow problems. Another reason for such a discrepancy can be
9 traced back to the order of accuracy of the numerical schemes implemented for the discretization
10 of the governing equations.
11
12
13
14
15
16
17
18
19
20
21

22 **4.4. Single rising bubble (case 6)**

23
24
25 To further assess the accuracy and consistency of the improved VOF model in solving
26 multiphase flows with high density contrast, the numerical simulation of the single bubble rising
27 in quiescent liquid is considered here as a last benchmark problem. This canonical test case was
28 originally introduced by Sussman et al. [19] and was then adopted by Almasi et al. [90],
29 Kruisbrink et al. [91] and Zainali et al. [92] to check the performance of Smoothed particle
30 hydrodynamics (SPH) method in dealing with the multi-fluid flows. Fig. 1 illustrates a schematic
31 sketch corresponding to the initial setup of the problem where a circular bubble with density and
32 viscosity of $\rho_L = 1.0 \text{ Kg m}^{-3}$ and $\mu_L = 1.106 \text{ Kg m}^{-1} \text{ s}^{-1}$ is located at $[1.5H, 1H]$ where
33 $H = 2R_0 = 1m$ represents the initial diameter of the bubble. The calculations are performed in a
34 rectangular duct $[3H, 5H]$ filled with water as a secondary phase ($\rho_H = 1000.0 \text{ Kg m}^{-3}$ and
35 $\mu_H = 3.130 \text{ Kg m}^{-1} \text{ s}^{-1}$). The pertinent parameters for this canonical test case are density ratio
36 $\rho_H / \rho_L = 1000$, viscosity ratio $\mu_H / \mu_L = 2.828$, Reynolds ($\text{Re} = \rho_H 2R \sqrt{2gR} / \mu_H = 1000$) and
37 Bond ($\text{Bo} = \rho_H g (2R)^2 / \sigma = 200$) numbers with $g = 9.8 \text{ ms}^{-2}$ stands for the acceleration of
38 gravity. No-slip boundary condition ($\mathbf{u} = 0$) is applied on all rigid walls and the effects of
39
40
41
42
43
44
45
46
47
48
49
50
51
52
53
54
55
56
57
58
59
60
61

1
2
3
4 surface tension force ($\sigma = 49 \text{ Kgs}^{-2}$) is taken into account. The uniform grid size of 450×750 is
5
6
7 used for the simulation and obtained results in terms of volume fraction field with selected
8
9 pressure contours are depicted in Fig. 11. Generally, the morphology and dynamics behavior of
10
11 the rising bubble strongly depend on the magnitudes of the Reynolds and Bond numbers such
12
13 that high surface tension (or low Bond number) and viscous (low Reynolds number) forces
14
15 prevent the bubble from twisting, and tend to keep the bubble circular in shape, accordingly
16
17 [93]. As seen from the figure, due to the existence of density gradient, the stationary bubble rises
18
19 up under the action of buoyancy force while the water descends downward following the
20
21 direction of gravity in the close proximity of the vertical walls, producing a pair of vortex rings
22
23 behind the gas phase ($0 \leq T \leq 1.062$). This mechanism causes the bubble shape undergoes
24
25 moderate dynamical change to form the well-known apple-like structure as documented by
26
27 Hysing et al. [94]. As time passes ($1.062 < T \leq 3.514$), the downwilling water motion with the
28
29 aid of unsteady vortex shedding begin to squeeze the bubble which results in the formation of the
30
31 horseshoe-shaped structure within the container. Once the bubble is pierced from the center, the
32
33 inertial force acting on the bubble decreases and consequently the surface tension force which is
34
35 more pronounced in regions with high interface curvature starts to play its role and subsequently
36
37 tear the main body. In this circumstance ($3.514 < T \leq 5.312$), the air bubble broadens, and the
38
39 horseshoe shape eventually splits into three main segments. This stage may be referred to as the
40
41 “*quasi terminal condition*” describing the morphology of a rising bubble where the piercing
42
43 phenomenon, detachment of two satellite bubbles, and reduction in bubble velocity are come to
44
45 pass sequentially in a short period of time [95]. However, as time progressed, the shape of the
46
47 bubble becomes more stable and flatter which signifies that the unsteady process starts to reach
48
49 its terminal velocity and hemispherical state where all relevant forces such as drag, gravity,
50
51
52
53
54
55
56
57
58
59
60
61

1
2
3
4 surface tension, buoyancy and viscosity are in hydraulic equilibrium. This assertion is well
5 supported by profiles of the interface positions plotted in Fig. 12 where due to the existence of
6 the weak fluid circulation and wake shedding, the minimum location of the two daughter bubbles
7 remains almost unchanged during the period time of $5.312 < T \leq 8.854$.
8
9

10
11
12
13
14
15 Coming to the comparison of the global characteristics of the bubble rising in Fig. 12, there is
16 satisfactory agreement between results of present work and those reported by Almasi et al. [90],
17 Kruisbrink et al. [91]. Moreover, the smoothness of the interface in the zoomed-in view of the
18 grid near the trailing edge of the main bubble confirms the capability of the TVD convection
19 scheme in capturing steep gradients without generating spurious oscillations or smearing.
20 Finally, the minimum and maximum positions of the bubble versus non-dimensional time are
21 also provided in Fig. 12 as additional information which may be used by scholars for
22 validation/verification purposes.
23
24
25
26
27
28
29
30
31
32
33

34 35 **5. Results and discussion**

36
37
38 In the previous section, the accuracy and versatility of the enhanced version of the VOF model
39 proposed by Garoosi et al. [51] were further verified against a series of challenging multi-fluid
40 flow problems. However, from the numerical viewpoint, validation of CFD codes is of the great
41 significant and has become a crucial part of the modelling process. As the number of users and
42 programmers increases, the need for new benchmark solutions has received a great deal of
43 attention by scientific community. Thus, at this stage, the verified VOF model will be employed
44 to examine and analyze two new multiphase problems namely merging of two rising bubbles
45 with different densities and diameters. The newly introduced benchmark solutions in the scope of
46
47
48
49
50
51
52
53
54
55
56
57
58
59
60
61
62
63
64
65

multifluid flows can provide a reliable dataset for validation of numerical models and shed more light on the coalescence process of the rising bubbles.

5.1. Merging of two rising bubbles with different densities and diameters (cases 7 & 8)

The configurations of two new benchmark solutions are depicted in Fig. 1. As can be seen, the calculations in both cases are performed in a rectangular container with size of $[H, 2.2H]$ where $H = 1m$ represents the width of the enclosure. The enclosure is filled with heavy fluid with nominal density and viscosity of $\rho_H = 1000 Kg m^{-3}$ and $\mu_H = 20 Kg m^{-1} s^{-1}$ where two circular bubbles with physical properties of $\rho_M = 500 Kg m^{-3}$, $\rho_L = 250 Kg m^{-3}$, $\mu_M = 10 Kg m^{-1} s^{-1}$ and $\mu_L = 5 Kg m^{-1} s^{-1}$ are located at $[0.5m, 0.5m]$ and $[0.5m, 1.1m]$, respectively. The subscripts H, M and L stand for the three immiscible Newtonian fluids namely Heavy, Middle and Lighter, respectively. The initial diameters of two bubbles in case 7 are set as $R_1 = 0.2m$ and $R_2 = 0.3m$ whereas these values in case 8 are $R_1 = 0.3m$ and $R_2 = 0.2m$. The morphological evolution and hydrodynamic characteristics of the problems under consideration is governed by Reynolds and Froude numbers defined as $Re = (2R_{max})U_0/\nu_H = \sqrt{g}(2R_{max})^{3/2}/\nu_H = 90$ and $Fr = U_0/\sqrt{g2R_{max}} = 1.0$ where ν_H , U_0 and R_{max} denote kinematic viscosity ($\nu_H = \nu_H = \nu_H = 0.02$), reference velocity and maximum radius of the bubbles within the computational domain ($R_{max} = 0.3m$). Inspired by works of Pan et al. [96] and Zhao et al. [97], in order to reach sever topological changes, the effects of surface tension force are not taken into consideration ($\sigma = 0$). The simulations are carried out on uniform distributed grid of 350×770 and no-slip boundary condition ($\vec{\mathbf{u}} = 0$) is imposed on all rigid walls. All working fluid including dense liquid (H) and bubbles (M, L) are assumed to be stationary at the initial state ($p = 0, \mathbf{u} = 0$)

1
2
3
4). The shape evolution mechanism of rising bubbles in a quiescent liquid with corresponding
5
6 velocity contours are portrayed in Figs. 13-16. Generally, from the wave theory point of the
7
8 view, the dynamic behavior of the rising bubble in a stagnant Newtonian liquid subjected to the
9
10 gravitational acceleration can be divided into three distinct stages namely: (1) linear stage where
11
12 the buoyancy force is dominant and fluid flow is characterized by the development of two
13
14 primary vortices, (2) weakly or quasi-linear stage where the bubble motion decelerates and the
15
16 resistance drag by the surrounding liquid becomes comparable by the buoyancy force, and (3)
17
18 fully non-linear stage where the final shape of the bubble is controlled and limited by viscous
19
20 drag and transport phenomenon starts to obey the Stokes law [98]. The snapshots of bubbles
21
22 shapes at six different time instants in Figs. 13-16 illustrate that, in early stages of impulsive
23
24 motion ($0 \leq T \leq 0.7$), the buoyancy force induced by the density gradients causes both bubbles
25
26 in cases 7 and 8 to travel upward while the dense fluid sinks downward in vicinity of the vertical
27
28 walls, leading to the development of a pair of counter-rotating eddies at the sides of the bubbles.
29
30 The corresponded velocity contours in Figs. 14 and 15 reveal that as time elapses ($0.7 < T \leq 1.5$),
31
32 due to lower flow resistance drag, the flow acceleration and magnitude of the vertical velocity
33
34 are intensified. This mechanism is accompanied by the invigoration of the downward jet current
35
36 of the surrounding liquid beneath the leading bubbles, which in turn causes the primary vortices
37
38 to move towards the region behind the leading bubbles, promoting the emergence of the prolate
39
40 shape. At this stage, the formation of the wake region between two bubbles becomes more
41
42 prominent and consequently some secondary vortices are appeared inside the bubbles. After a
43
44 fast acceleration, during the period of $1.5 < T \leq 2.5$, owing to the enhancement in the friction
45
46 drag and shear force at the poles of the bubbles, the motion of the fluids flow slows down and the
47
48 upper bubble in both cases begins to transform into the shape of a dimpled ellipsoidal-cap. It is
49
50
51
52
53
54
55
56
57
58
59
60
61

1
2
3
4 constantly perceived that, the well-developed vortices encourage the leading bubbles to elongate
5
6 longitudinally and envelop the lower bubbles. In these circumstances, due to the shielding effects
7
8 of the wake flow on rear of the leading bubbles (M), the trailing bubbles (L) undergo sever
9
10 deformation and start to be swallowed by the primary bubbles. It can be seen from Figs. 14 and
11
12 15 that, in the later rising moments ($2.5 < T \leq 5.5$) where the buoyancy effects are less important
13
14 and viscous force is leading the fluid flow, the magnitude of the non-dimensional velocity
15
16 components remains almost unaltered. This physical model is the strong indication of the onset
17
18 of the terminal condition and non-linearity within the fluid domain. It is evident that at this stage,
19
20 the merged bubbles in both cases move with their constant velocity while deforming into the
21
22 complex patterns. However, as pointed out before, if the effects of surface tension force were
23
24 considered, the distortion of the bubbles shapes would become much less significant than the
25
26 results obtained in Fig. 13.
27
28
29
30
31
32

33
34 The time histories of the maximum positions of the bubbles fronts are displayed in Fig. 16. The
35
36 close inspection of the figure shows that, although the global variations of the interfaces profiles
37
38 in both cases are relatively similar and follow the general trend of the curves, the coalescence
39
40 time is slightly different. It can be seen that, in case 8 the tips of the leading and trailing bubbles
41
42 meet each other at $T \approx 4.4$ while this course of event occurs at $T \approx 5.5$. This behavior can be
43
44 partially originated from the stronger wake region generated in case 8 which causes the trailing
45
46 bubble to rise faster compared to the one in case 7. Another reason behind this behavior can be
47
48 attributed to the larger diameter of the lower bubble in case 8 which in turn leads to the stronger
49
50 buoyancy force and lower shear force at the beginning of the evolution. This assertion is well
51
52 supported by Figs. 14 and 15 where the maximum vertical velocity in the entire evolution in case
53
54 8 is considerably higher than that of case 7. In fact, these observations suggest that, the diameter
55
56
57
58
59
60
61

1
2
3
4 and density of the leading and trailing bubbles have significant impact on the coalescence
5
6 process and morphological characteristics of dual bubbles rising phenomenon.
7
8

9 10 **6. Conclusions**

11
12
13 In the present work, the accuracy and stability of an enhanced version of the Volume-Of-Fluid
14 (VOF) model proposed by Garoosi et al. [51] are further tested against a series of challenging
15 benchmark cases including draining of liquids from the storage tank (tank draining), single rising
16 bubble, three-phase Rayleigh-Taylor Instability and dam-break flows over dry and wet beds. In
17 the second part of the study, the verified VOF model is adopted to examine and analyze the
18 transient evolution of two rising bubbles with different densities and diameters, aiming to
19 establish the state-of-the-art benchmark solutions and up-to-date dataset for the verification and
20 validation of CFD codes. The results of the numerical analysis led to the following conclusions:
21
22
23
24
25
26
27
28
29
30
31

- 32
33 • It is found that, the enhanced VOF model allows accurate and consistent predictions of
34 non-linear free-surface flows involving plunging wave breaking, large slamming events,
35 impact pressure and interface rupture/coalescence.
36
37
- 38 • The results show that, the sharpness of the interface can be successfully preserved by
39 implementing third-order TVD bounded convection scheme.
40
41
- 42 • The obtained results show that, the third-order TVD bounded convection scheme can
43 efficiently alleviate the numerical diffusion, thereby eliminating interface smearing.
44
45
- 46 • Through the numerical modelling of the three-phase Rayleigh-Taylor Instability, it is
47 found that, the enhanced VOF model is capable of resolving multi-fluid flows with sever
48 topological changes in comparison with Lgrangian mesh-free particle model (MPS).
49
50
51
52
53
54
55
56
57
58
59
60
61

- It is found that, the implementation of the hybrid PISOC algorithm can efficiently stabilize the numerical solutions and provide smoother pressure distribution in terms of both space and time.
- The results of the single bubble rising with high density ratio vividly confirm that, the proposed numerical approach can successfully address the problem of physical discontinuities particularly when flow-to-grid skewness is substantial.
- The results of merging of two rising bubbles with different densities illustrate that, the enhanced VOF model is capable of handling non-linear multi-fluid flows with large deformation and twisting
- The numerical simulation of buoyancy-driven merging of two bubbles with different densities reveal that, the initial diameters of the leading and trailing bubbles have notable impact on the coalescence process and terminal bubbles shape.
- It is found that, in the problem of buoyancy-driven merging of two bubbles, the shape and deformation of the lower bubble are significantly influenced by the diameter and wake of the upper bubble.

Supplementary material

In order to provide a comprehensive understanding of simulated benchmark problems, seven different video files associated with cases 1 to 6 are provided as supplementary material.

Declaration of Competing Interest

The authors declare that they have no known competing financial interests or personal relationships that could have appeared to influence the work reported in this paper.

1
2
3
4 **CRedit authorship contribution statement**

5
6
7 **Farooqh Garoosi:** Conceptualization, Methodology, FORTRAN Code development, Validation,
8 Visualization, Writing-Original Draft.
9

10
11 **Tarek Merabtene:** Investigation, Validation, Writing-Review & Editing.
12

13
14 **Tew-Fik Mahdi:** Supervision, Funding acquisition, Validation, Writing-Review & Editing.
15
16

17 **Acknowledgment**
18

19
20
21 This research was funded, in part, by a National Science and Engineering Research Council
22 (NSERC) Discovery Grant for the co-author Tew-Fik Mahdi, application No: RGPIN-2021-
23 03272.
24
25
26
27

28
29 **Appendix A** (Hybrid PISO-Chorin algorithm for solving Pressure-Poisson equation)
30
31

32
33 A methodology for derivation of the hybrid PISOC algorithm which is the hybrid version of the
34 standard PISO algorithm [56] and Chorin's model (two-step projection method) [57] is
35 elaborated along this appendix. The PISOC algorithm was originally pioneered by Garoosi et al.
36 [51] for decoupling of velocity and pressure in Navier-Stokes equations on the staggered grid
37 arrangement, aiming to eliminate numerical oscillation from the computational domain in
38 incompressible multiphase flows and to speed up convergence rate of implicit iteration process.
39
40 As outlined in section 3, the convection terms in the governing equations are discretized using
41 the third-order TVD bounded scheme while the second-order central differencing scheme is
42 applied for the treatment of the diffusion terms. Meanwhile, the pressure gradient term is
43 approximated by means of the linear interpolation between two immediate nodes located on the
44 momentum cell faces [71]. By implementing the above differencing schemes, a finite volume
45
46
47
48
49
50
51
52
53
54
55
56
57
58
59
60
61
62
63
64
65

1
2
3
4 discretization of the momentum equations can be expressed in the form of a linear algebraic
5
6 equation as:

$$7 \quad a_{ip} \mathbf{u}_p = \sum a_{np} \mathbf{u}_{np} + S_u + S_t - A_p (p_p - p_{np}) \quad (A1)$$

8
9
10 where the subscript nb represent the neighboring velocity nodes and S_u is the volumetric source
11
12 term. a_{ip} and a_{np} are the diagonal and neighbour coefficients which represents the implicit form
13
14 of the convection and diffusion variables together with the transient term of $\partial \rho \mathbf{u} / \partial t$. As stated
15
16 before, in order to ensure second-order temporal accuracy of the numerical simulation, the *three-*
17
18 *time-levels* scheme proposed by Kim et al. [72] is utilized for discretization of the transient term
19
20 as:

$$21 \quad \frac{\partial \rho \mathbf{u}}{\partial t} = \frac{3(\rho \mathbf{u})_p^{n+1} - 4(\rho \mathbf{u})_p^n + (\rho \mathbf{u})_p^{n-1}}{2\Delta t} \quad (A2)$$

22
23 By substituting Eq. (A2) into Eq. (A1), the central coefficient a_{ip} and source term S_t for the
24
25 transient flow can be written as:

$$26 \quad a_{ip} = a_p + \frac{3\rho_p^{n+1}}{2\Delta t} \Delta x \Delta y \quad (A3)$$

$$27 \quad S_t = \frac{4(\rho \mathbf{u})_p^n - (\rho \mathbf{u})_p^{n-1}}{2\Delta t} \Delta x \Delta y \quad (A4)$$

28
29 where a_p is the central coefficient arising from the discretization of the linearized steady-state
30
31 Navier-Stokes equations (for more details see previous works of Tuković et al. [99]). To initiate
32
33 the PISOC algorithm and to compute the coefficients and constant terms in the momentum
34
35 discrete equation, the initial guessed value of \mathbf{u}^* is assigned for velocity components. Ideally, the
36
37 discretized momentum equations based on the guessed flow variables and correct pressure
38
39 distribution (p^{n+1}) can fulfill both momentum and mass laws as [71]:

$$\mathbf{u}_p^{n+1} = \frac{\sum a_{np} \mathbf{u}_{np}^* + S_u + S_t}{a_{ip}} - \frac{A_p (p_p^{n+1} - p_{np}^{n+1})}{a_{ip}} \quad (\text{A5})$$

It should be noted that, at this stage, all constant coefficients namely a_{np} , a_{ip} and A_p are evaluated using the initial guess, hence the terminology “*operator splitting*” [100]. By introducing the pseudo velocity (\mathbf{u}) into the methodology and eliminating the pressure gradient term from Eq. (A5), the first predictor-corrector step of the algorithm related to the Chorin’s model (two-step projection model) can be accomplished as [101]:

$$\mathbf{u} = \frac{\sum a_{np} \mathbf{u}_{np}^* + S_u + S_t}{a_{ip}} \quad (\text{A6})$$

$$\mathbf{u}_p^{n+1} = \mathbf{u} - \frac{2d_{ip} (p_p^{n+1} - p_{np}^{n+1})}{3} \quad (\text{A7})$$

where $d_{ip} = A_p / a_{ip}$. By substituting Eq. (A8) into the following discretised continuity equation [102]:

$$[(\rho u A)_e - (\rho u A)_w] + [(\rho v A)_n - (\rho v A)_s] = 0 \quad (\text{A8})$$

The following PPE equation can be obtained:

$$\begin{aligned} a_{i,j} P_{i,j}^{n+1} &= a_{i+1,j} P_{i+1,j}^{n+1} + a_{i-1,j} P_{i-1,j}^{n+1} + a_{i,j+1} P_{i,j+1}^{n+1} + a_{i,j-1} P_{i,j-1}^{n+1} + \frac{3}{2} b_{i,j} - \frac{3}{2} \left(\frac{3\rho_p^{n+1} - 4\rho_p^n + \rho_p^{n-1}}{2\Delta t \rho_p^{n+1}} \Delta x \Delta y \right) \\ a_{i,j} &= a_{i+1,j} + a_{i-1,j} + a_{i,j+1} + a_{i,j-1} \\ a_{i+1,j} &= d_{i+1,j} \Delta y, \quad a_{i-1,j} = d_{i,j} \Delta y \\ a_{i,j+1} &= d_{i,j+1} \Delta x, \quad a_{i,j-1} = d_{i,j} \Delta x \\ b_{i,j} &= u_{i,j} \Delta y - u_{i+1,j} \Delta y + \hat{v}_{i,j} \Delta x - \hat{v}_{i,j+1} \Delta x \end{aligned} \quad (\text{A9})$$

where $b_{i,j}$ stands for the mass imbalance arising from the pseudo velocities. Once the pressure distribution is computed, the pseudo velocity field can be modified using Eq. (A7). At this stage, it is important to note that, contrary to the fully-iterative version of PISO or PIMPLE algorithm, in order to achieve some prescribed level of accuracy, the iteration process is only applied to Eq.

(A9) rather than extending it throughout the calculations, making the proposed PISOC algorithm more computationally efficient in comparison with traditional SIMPLE, SIMPLER, SIMPLEC, PISO and PIMPLE algorithms [55]. Note that, Eqs. (A1) to (A9) are part of the standard Chorin's model and also correspond to the SIMPLER algorithm [71].

To initiate the second part of the methodology related to the PISO algorithm, one can assume that, the pressure and velocity values predicted from the previous stage still cannot satisfy the conservation of mass after a prescribed number of iterations applied on Eq. (9). Thus, the superscripts of these variables (p^{n+1}, u^{n+1}) are replaced by (p^*, u^{**}). By substituting the semi-corrected values of p^* and u^{**} into the Eq. (A1), the discrete momentum equation for the current time step may be written as:

$$a_{ip} \mathbf{u}_p^{**} = \sum a_{np} \mathbf{u}_{np}^{**} + S_u + S_t - A_p (p_p^* - p_{np}^*) \quad (\text{A10})$$

where \mathbf{u}^{**} stands for the updated (modified) velocity field. However, by subtracting Eq. (A10) from (A1) and introducing the incremental pressure (p') and velocity variables (\mathbf{u}'), the following formulations can be achieved:

$$a_{ip} (\mathbf{u}_p - \mathbf{u}_p^{**}) = \sum a_{np} (\mathbf{u}_{np} - \mathbf{u}_{np}^{**}) - A_p [(p_p - p_p^*) - (p_{np} - p_{np}^*)] \quad (\text{A11})$$

$$p = p^* + p' \quad (\text{A12})$$

$$\mathbf{u} = \mathbf{u}^{**} + \mathbf{u}'$$

$$a_{ip} (\mathbf{u}'_p) = -A_p (p'_p - p'_{np}) \quad (\text{A13})$$

$$\mathbf{u} = \mathbf{u}^{**} + \mathbf{u}'_p = \mathbf{u}^{**} - \frac{A_p (p'_p - p'_{np})}{a_{ip}} \quad (\text{A14})$$

Note that, similar to the original PISO algorithm, for the sake of simplicity, the summation over the adjacent velocity points is omitted here ($\sum a_{np} (\mathbf{u}_{np} - \mathbf{u}_{np}^{**}) = \sum a_{np} (\mathbf{u}'_{np}) \approx 0$). Substituting Eq.

(A14) into the discretized continuity equation yields the first system of discrete pressure-correction equation as:

$$a_{i,j}P'_{i,j} = a_{i+1,j}P'_{i+1,j} + a_{i-1,j}P'_{i-1,j} + a_{i,j+1}P'_{i,j+1} + a_{i,j-1}P'_{i,j-1} + b_{i,j} - \frac{3\rho_p^{n+1} - 4\rho_p^n + \rho_p^{n-1}}{2\Delta t \rho_p^{n+1}} \Delta x \Delta y \quad (\text{A15})$$

$$\begin{aligned} a_{i,j} &= a_{i+1,j} + a_{i-1,j} + a_{i,j+1} + a_{i,j-1} \\ a_{i+1,j} &= d_{i+1,j} \Delta y, \quad a_{i-1,j} = d_{i,j} \Delta y \\ a_{i,j+1} &= d_{i,j+1} \Delta x, \quad a_{i,j-1} = d_{i,j} \Delta x \\ b_{i,j} &= u_{i,j}^{**} \Delta y - u_{i+1,j}^{**} \Delta y + \tilde{v}_{i,j}^{***} \Delta x - \tilde{v}_{i,j+1}^{***} \Delta x \end{aligned} \quad (\text{A16})$$

Once the above equation is solved, the velocity and pressure fields can be modified via Eqs. (A12) and (A14) as:

$$\begin{aligned} p &= p^* + \alpha_{p1} p' \\ \mathbf{u} &= \mathbf{u}^{**} - \frac{A_p (p'_p - p'_{np})}{a_{ip}} \end{aligned} \quad (\text{A17})$$

where α_{p1} denotes the first under-relaxation factor which is taken as unity in the current work.

Once again it is assumed that the newly corrected velocity (\mathbf{u}) field obtained from Eq. (17) is still not divergence free ($\nabla \cdot \mathbf{u} \neq 0$) and therefore cannot satisfy the continuity equation rigorously.

This assumption means that before advancing to the next time step ($n+1$), the second pressure-correction step as a main part of the PISO algorithm is needed to reach a satisfactory degree of consistency. Thus, similar to the previous step, the superscripts of the modified velocity and pressure fields in Eq. (A17) are replaced by $\mathbf{u} \rightarrow \mathbf{u}^{***}$ and $p \rightarrow p^{**}$. By substituting the second semi-corrected velocity (\mathbf{u}^{***}) and pressure (p^{**}) values into the momentum equation, the third

modified velocity (\mathbf{u}^{***}) can be obtained as:

$$\mathbf{u}_p^{***} = \frac{\sum a_{np} \mathbf{u}_{np}^{***} + S_u + S_t}{a_{ip}} - \frac{A_p (p_p^{**} - p_{np}^{**})}{a_{ip}} \quad (\text{A18})$$

1
2
3
4 It is important to note that, contrary to the classical PISO algorithm, due to the utilization of
5
6 modified velocity and pressure values in momentum equation, the central (a_{ip}) and neighbor (
7
8 a_{np}) coefficients in Eq. (A10) are replaced by the updated coefficients a_{ip} and a_{np} in Eq. (A18).
9
10
11 Our results have shown that, this modification has a significant impact on the accuracy and
12
13 convergence rate of numerical solution in dealing with the convection-dominated flows. To
14
15 terminate the methodology, it is assumed that the correct pressure field (p^{n+1}) with the aid of the
16
17 newly updated velocity field (\mathbf{u}^{***}) can accurately ensure the mass and momentum conservation
18
19 at each computation grid as:
20
21
22
23
24
25
26

$$\mathbf{u}^{n+1} = \frac{\sum a_{np} \mathbf{u}_{np}^{***} + S_u + S_t}{a_{ip}} - \frac{A_p (p_p^{n+1} - p_{np}^{n+1})}{a_{ip}} \quad (\text{A19})$$

27
28 By subtracting Eq. (A19) from (A18) and defining the second incremental pressure variable (p''
29
30
31
32
33
34
35
36
37
38
39
40
41
42
43
44
45
46
47
48
49
50
51
52
53
54
55
56
57
58
59
60
61
62
63
64
65
66
67
68
69
70
71
72
73
74
75
76
77
78
79
80
81
82
83
84
85
86
87
88
89
90
91
92
93
94
95
96
97
98
99
100
101
102
103
104
105
106
107
108
109
110
111
112
113
114
115
116
117
118
119
120
121
122
123
124
125
126
127
128
129
130
131
132
133
134
135
136
137
138
139
140
141
142
143
144
145
146
147
148
149
150
151
152
153
154
155
156
157
158
159
160
161
162
163
164
165
166
167
168
169
170
171
172
173
174
175
176
177
178
179
180
181
182
183
184
185
186
187
188
189
190
191
192
193
194
195
196
197
198
199
200
201
202
203
204
205
206
207
208
209
210
211
212
213
214
215
216
217
218
219
220
221
222
223
224
225
226
227
228
229
230
231
232
233
234
235
236
237
238
239
240
241
242
243
244
245
246
247
248
249
250
251
252
253
254
255
256
257
258
259
260
261
262
263
264
265
266
267
268
269
270
271
272
273
274
275
276
277
278
279
280
281
282
283
284
285
286
287
288
289
290
291
292
293
294
295
296
297
298
299
300
301
302
303
304
305
306
307
308
309
310
311
312
313
314
315
316
317
318
319
320
321
322
323
324
325
326
327
328
329
330
331
332
333
334
335
336
337
338
339
340
341
342
343
344
345
346
347
348
349
350
351
352
353
354
355
356
357
358
359
360
361
362
363
364
365
366
367
368
369
370
371
372
373
374
375
376
377
378
379
380
381
382
383
384
385
386
387
388
389
390
391
392
393
394
395
396
397
398
399
400
401
402
403
404
405
406
407
408
409
410
411
412
413
414
415
416
417
418
419
420
421
422
423
424
425
426
427
428
429
430
431
432
433
434
435
436
437
438
439
440
441
442
443
444
445
446
447
448
449
450
451
452
453
454
455
456
457
458
459
460
461
462
463
464
465
466
467
468
469
470
471
472
473
474
475
476
477
478
479
480
481
482
483
484
485
486
487
488
489
490
491
492
493
494
495
496
497
498
499
500
501
502
503
504
505
506
507
508
509
510
511
512
513
514
515
516
517
518
519
520
521
522
523
524
525
526
527
528
529
530
531
532
533
534
535
536
537
538
539
540
541
542
543
544
545
546
547
548
549
550
551
552
553
554
555
556
557
558
559
560
561
562
563
564
565
566
567
568
569
570
571
572
573
574
575
576
577
578
579
580
581
582
583
584
585
586
587
588
589
590
591
592
593
594
595
596
597
598
599
600
601
602
603
604
605
606
607
608
609
610
611
612
613
614
615
616
617
618
619
620
621
622
623
624
625
626
627
628
629
630
631
632
633
634
635
636
637
638
639
640
641
642
643
644
645
646
647
648
649
650
651
652
653
654
655
656
657
658
659
660
661
662
663
664
665
666
667
668
669
670
671
672
673
674
675
676
677
678
679
680
681
682
683
684
685
686
687
688
689
690
691
692
693
694
695
696
697
698
699
700
701
702
703
704
705
706
707
708
709
710
711
712
713
714
715
716
717
718
719
720
721
722
723
724
725
726
727
728
729
730
731
732
733
734
735
736
737
738
739
740
741
742
743
744
745
746
747
748
749
750
751
752
753
754
755
756
757
758
759
760
761
762
763
764
765
766
767
768
769
770
771
772
773
774
775
776
777
778
779
780
781
782
783
784
785
786
787
788
789
790
791
792
793
794
795
796
797
798
799
800
801
802
803
804
805
806
807
808
809
810
811
812
813
814
815
816
817
818
819
820
821
822
823
824
825
826
827
828
829
830
831
832
833
834
835
836
837
838
839
840
841
842
843
844
845
846
847
848
849
850
851
852
853
854
855
856
857
858
859
860
861
862
863
864
865
866
867
868
869
870
871
872
873
874
875
876
877
878
879
880
881
882
883
884
885
886
887
888
889
890
891
892
893
894
895
896
897
898
899
900
901
902
903
904
905
906
907
908
909
910
911
912
913
914
915
916
917
918
919
920
921
922
923
924
925
926
927
928
929
930
931
932
933
934
935
936
937
938
939
940
941
942
943
944
945
946
947
948
949
950
951
952
953
954
955
956
957
958
959
960
961
962
963
964
965
966
967
968
969
970
971
972
973
974
975
976
977
978
979
980
981
982
983
984
985
986
987
988
989
990
991
992
993
994
995
996
997
998
999
1000

$$\mathbf{u}^{n+1} - \mathbf{u}_p^{***} = \frac{\sum a_{np} \mathbf{u}_{np}^{***} + S_u + S_t}{a_{ip}} - \frac{\sum a_{np} \mathbf{u}_{np}^{***} + S_u + S_t}{a_{ip}} - \frac{A_p (p_p^{n+1} - p_{np}^{n+1})}{a_{ip}} + \frac{A_p (p_p^{**} - p_{np}^{**})}{a_{ip}} \quad (\text{A20})$$

$$p^{n+1} = p^{**} + \alpha_{p2} p'' \quad (\text{A21})$$

$$\mathbf{u}^{n+1} = \mathbf{u}_p^{***} + \frac{\sum a_{np} (\mathbf{u}_{np}^{***} - \mathbf{u}_{np}^{***})}{a_{ip}} - \frac{A_p (p_p'' - p_{np}'')}{a_{ip}} \quad (\text{A22})$$

where $\alpha_{p2} = 1$ is the second under-relaxation factor. Substitution of \mathbf{u}^{n+1} in the discretized
continuity equation results in the second partial differential equation for the incremental pressure
given by:

$$a_{i,j} P''_{i,j} = a_{i+1,j} P''_{i+1,j} + a_{i-1,j} P''_{i-1,j} + a_{i,j+1} P''_{i,j+1} + a_{i,j-1} P''_{i,j-1} + \tilde{b}_{i,j} + \tilde{b}_{i,j} - \frac{3\rho_p^{n+1} - 4\rho_p^n + \rho_p^{n-1}}{2\Delta t \rho_p^{n+1}} \Delta x \Delta y \quad (\text{A23})$$

$$\begin{aligned}
a_{i,j} &= a_{i+1,j} + a_{i-1,j} + a_{i,j+1} + a_{i,j-1} \\
a_{i+1,j} &= d_{i+1,j}\Delta y, \quad a_{i-1,j} = d_{i,j}\Delta y \\
a_{i,j+1} &= d_{i,j+1}\Delta x, \quad a_{i,j-1} = d_{i,j}\Delta x \\
\tilde{b}_{i,j} &= u_{i,j}^{***}\Delta y - u_{i+1,j}^{***}\Delta y + \tilde{v}_{i,j}^{***}\Delta x - \tilde{v}_{i,j+1}^{***}\Delta x \\
\tilde{b}_{i,j} &= \left(\frac{\sum a_{np}(u_{np}^{***} - u_{np}^{***})}{a_{ip}} \right)_{i,j} \Delta y - \left(\frac{\sum a_{np}(u_{np}^{***} - u_{np}^{***})}{a_{ip}} \right)_{i+1,j} \Delta y \\
&+ \left(\frac{\sum \widetilde{a_{np}}(\tilde{v}_{np}^{***} - v_{np}^{***})}{a_{ip}} \right)_{i,j} \Delta x - \left(\frac{\sum \widetilde{a_{np}}(\tilde{v}_{np}^{***} - v_{np}^{***})}{a_{ip}} \right)_{i,j+1} \Delta x
\end{aligned} \tag{A24}$$

Once the second pressure correction equation is solved, the exact velocity and pressure values can be computed via Eqs. (A21) and (A22). Having determined the correct velocity field, the volume fraction equation is solved and calculation is then transferred to the next time step where the updated physical quantities will be utilized as an initial guess values for the next level. However, before ending this discussion, it is worthwhile mentioning that, in the standard PISO-algorithm, Issa [56] ideally assumed that the twice-improved velocity field (\mathbf{u}^{***}) emerged as a source term ($\tilde{b}_{i,j}$) on the right hand side of Eq. (A24) is sufficiently accurate to fulfill zero-divergence constraint ($\nabla \cdot \mathbf{u}^{***} = 0, \tilde{b}_{i,j} = 0$). However, our results have revealed that this assumption is not necessarily valid such that the strict enforcement of the continuity constraint via the direct imposition of $\nabla \cdot \mathbf{u}^{***} = 0$ (or $\tilde{b}_{i,j} = 0$) in Eq. (A24) may lead to unphysical pressure/velocity fluctuation in highly nonlinear multi-fluid flow problems.

References

- [1] M.S. Alagha, P. Szentannai, Experimentally-assessed multi-phase CFD modeling of segregating gas-solid fluidized beds, Chem. Eng. Res. Des. (2021).
- [2] E. Zhou, B. Lv, X. Deng, X. Qin, C. Fang, Hydrodynamic and separation performance of gas–solid separation fluidized bed with two-size-orifice distributor, Chem. Eng. Res. Des. 168 (2021) 397–410.

- 1
2
3
4 [3] J.P. Moris, A.B. Kennedy, J.J. Westerink, Tsunami wave run-up load reduction inside a
5 building array, *Coast. Eng.* (2021) 103910.
6
7 [4] W.C. Moon, H.T. Puay, T.L. Lau, Robust and efficient 3-D numerical model for the
8 hydrodynamic simulation of tsunami wave on land, *Adv. Water Resour.* 146 (2020)
9 103762.
10
11 [5] E. Zhao, J. Sun, Y. Tang, L. Mu, H. Jiang, Numerical investigation of tsunami wave
12 impacts on different coastal bridge decks using immersed boundary method, *Ocean Eng.*
13 201 (2020) 107132.
14
15 [6] Q. Zhao, W. Ren, Z. Zhang, A Thermodynamically Consistent Model and Its
16 Conservative Numerical Approximation for Moving Contact Lines with Soluble
17 Surfactants, *ArXiv Prepr. ArXiv2104.02626.* (2021).
18
19 [7] H. Hao, J. Yu, Y. Song, F. Chen, T. Liu, Deformation and regimes of liquid column
20 during water exit of a partially submerged sphere using the front-tracking lattice
21 Boltzmann method, *J. Fluids Struct.* 99 (2020) 103152.
22
23 [8] C.-H. Lee, C. Xu, Z. Huang, A three-phase flow simulation of local scour caused by a
24 submerged wall jet with a water-air interface, *Adv. Water Resour.* 129 (2019) 373–384.
25
26 [9] J. García-Maribona, J.L. Lara, M. Maza, I.J. Losada, An efficient RANS numerical model
27 for cross-shore beach processes under erosive conditions, *Coast. Eng.* (2021) 103975.
28
29 [10] J. Mao, L. Zhao, Y. Di, X. Liu, W. Xu, A resolved CFD–DEM approach for the
30 simulation of landslides and impulse waves, *Comput. Methods Appl. Mech. Eng.* 359
31 (2020) 112750.
32
33 [11] G. Tryggvason, R. Scardovelli, S. Zaleski, *Direct numerical simulations of gas–liquid*
34 *multiphase flows*, Cambridge University Press, 2011.
35
36 [12] F. Gibou, D. Hyde, R. Fedkiw, Sharp interface approaches and deep learning techniques
37 for multiphase flows, *J. Comput. Phys.* 380 (2019) 442–463.
38
39 [13] N. Scapin, P. Costa, L. Brandt, A volume-of-fluid method for interface-resolved
40 simulations of phase-changing two-fluid flows, *J. Comput. Phys.* 407 (2020) 109251.
41
42 [14] K.K. So, X.Y. Hu, N.A. Adams, Anti-diffusion interface sharpening technique for two-
43 phase compressible flow simulations, *J. Comput. Phys.* 231 (2012) 4304–4323.
44
45 [15] T.J.R. Hughes, W.K. Liu, T.K. Zimmermann, Lagrangian-Eulerian finite element
46 formulation for incompressible viscous flows, *Comput. Methods Appl. Mech. Eng.* 29
47 (1981) 329–349.
48
49 [16] S.O. Unverdi, G. Tryggvason, A front-tracking method for viscous, incompressible, multi-
50 fluid flows, *J. Comput. Phys.* 100 (1992) 25–37.
51
52 [17] D.J. Torres, J.U. Brackbill, The point-set method: front-tracking without connectivity, *J.*
53 *Comput. Phys.* 165 (2000) 620–644.
54
55
56
57
58
59
60
61

- 1
2
3
4 [18] Q. Zhu, J. Yan, A mixed interface-capturing/interface-tracking formulation for thermal
5 multi-phase flows with emphasis on metal additive manufacturing processes, *Comput.*
6 *Methods Appl. Mech. Eng.* 383 (2021) 113910.
7
8
9 [19] M. Sussman, P. Smereka, S. Osher, A level set approach for computing solutions to
10 incompressible two-phase flow, *J. Comput. Phys.* 114 (1994) 146–159.
11
12 [20] C.W. Hirt, B.D. Nichols, Volume of fluid (VOF) method for the dynamics of free
13 boundaries, *J. Comput. Phys.* 39 (1981) 201–225. doi:10.1016/0021-9991(81)90145-5.
14
15 [21] C. Daskiran, X. Xue, F. Cui, J. Katz, M.C. Boufadel, Large eddy simulation and
16 experiment of shear breakup in liquid-liquid jet: Formation of ligaments and droplets, *Int.*
17 *J. Heat Fluid Flow.* 89 (2021) 108810.
18
19
20 [22] F. Bahmanpouri, M. Daliri, A. Khoshkonesh, M.M. Namin, M. Buccino, Bed compaction
21 effect on dam break flow over erodible bed; experimental and numerical modeling, *J.*
22 *Hydrol.* 594 (2021) 125645.
23
24 [23] A. Issakhov, Y. Zhandaulet, Numerical study of dam break waves on movable beds for
25 various forms of the obstacle by VOF method, *Ocean Eng.* 209 (2020) 107459.
26
27 [24] A. Issakhov, A. Borsikbayeva, The impact of a multilevel protection column on the
28 propagation of a water wave and pressure distribution during a dam break: Numerical
29 simulation, *J. Hydrol.* 598 (2021) 126212.
30
31 [25] L.C. Ngo, H.G. Choi, A multi-level adaptive mesh refinement for an integrated finite
32 element/level set formulation to simulate multiphase flows with surface tension, *Comput.*
33 *Math. with Appl.* 79 (2020) 908–933.
34
35 [26] X. Li, M. Liu, T. Dong, D. Yao, Y. Ma, VOF-DEM simulation of single bubble behavior
36 in gas-liquid-solid mini-fluidized bed, *Chem. Eng. Res. Des.* (2020).
37
38 [27] F. Gibou, R. Fedkiw, S. Osher, A review of level-set methods and some recent
39 applications, *J. Comput. Phys.* 353 (2018) 82–109.
40
41 [28] X. Yin, I. Zarihos, N.K. Karadimitriou, A. Raouf, S.M. Hassanizadeh, Direct simulations
42 of two-phase flow experiments of different geometry complexities using Volume-of-Fluid
43 (VOF) method, *Chem. Eng. Sci.* 195 (2019) 820–827.
44
45 [29] T. Marić, D.B. Kothe, D. Bothe, Unstructured un-split geometrical volume-of-fluid
46 methods—a review, *J. Comput. Phys.* 420 (2020) 109695.
47
48 [30] S.K. Choi, H.Y. Nam, M. Cho, A comparison of higher-order bounded convection
49 schemes, *Comput. Methods Appl. Mech. Eng.* 121 (1995) 281–301.
50
51 [31] D. Zhang, C. Jiang, D. Liang, L. Cheng, A review on TVD schemes and a refined flux-
52 limiter for steady-state calculations, *J. Comput. Phys.* 302 (2015) 114–154.
53
54 [32] B.B.M. Kassar, J.N.E. Carneiro, A.O. Nieckele, Curvature computation in volume-of-fluid
55 method based on point-cloud sampling, *Comput. Phys. Commun.* 222 (2018) 189–208.
56
57
58
59
60
61
62
63
64
65

- 1
2
3
4 [33] J.E. Pilliod Jr, E.G. Puckett, Second-order accurate volume-of-fluid algorithms for
5 tracking material interfaces, *J. Comput. Phys.* 199 (2004) 465–502.
6
7 [34] M. V Kraposhin, M. Banholzer, M. Pfitzner, I.K. Marchevsky, A hybrid pressure- based
8 solver for nonideal single- phase fluid flows at all speeds, *Int. J. Numer. Methods Fluids.*
9 88 (2018) 79–99.
10
11 [35] P. Bruno, G. Di Bella, M. De Marchis, Effect of the contact tank geometry on disinfection
12 efficiency, *J. Water Process Eng.* 41 (2021) 102035.
13
14 [36] J.P. Boris, D.L. Book, Flux-corrected transport. I. SHASTA, a fluid transport algorithm
15 that works, *J. Comput. Phys.* 11 (1973) 38–69.
16
17 [37] A. Harten, High resolution schemes for hyperbolic conservation laws, *J. Comput. Phys.*
18 135 (1997) 260–278.
19
20 [38] B.P. Leonard, Simple high- accuracy resolution program for convective modelling of
21 discontinuities, *Int. J. Numer. Methods Fluids.* 8 (1988) 1291–1318.
22
23 [39] P.K. Sweby, High resolution schemes using flux limiters for hyperbolic conservation
24 laws, *SIAM J. Numer. Anal.* 21 (1984) 995–1011.
25
26 [40] F. Kemm, A comparative study of TVD- limiters—well- known limiters and an
27 introduction of new ones, *Int. J. Numer. Methods Fluids.* 67 (2011) 404–440.
28
29 [41] J. Zhu, W. Rodi, A low dispersion and bounded convection scheme, *Comput. Methods*
30 *Appl. Mech. Eng.* 92 (1991) 87–96.
31
32 [42] P.H. Gaskell, A.K.C. Lau, Curvature- compensated convective transport: SMART, a new
33 boundedness- preserving transport algorithm, *Int. J. Numer. Methods Fluids.* 8 (1988)
34 617–641.
35
36 [43] V.G. Ferreira, R.A.B. De Queiroz, G.A.B. Lima, R.G. Cuenca, C.M. Oishi, J.L.F.
37 Azevedo, S. McKee, A bounded upwinding scheme for computing convection-dominated
38 transport problems, *Comput. Fluids.* 57 (2012) 208–224.
39
40 [44] J. Zhu, On the higher-order bounded discretization schemes for finite volume
41 computations of incompressible flows, *Comput. Methods Appl. Mech. Eng.* 98 (1992)
42 345–360.
43
44 [45] H. Jasak, H.G. Weller, A.D. Gosman, High resolution NVD differencing scheme for
45 arbitrarily unstructured meshes, *Int. J. Numer. Methods Fluids.* 31 (1999) 431–449.
46
47 [46] B. Van Leer, Towards the ultimate conservative difference scheme. II. Monotonicity and
48 conservation combined in a second-order scheme, *J. Comput. Phys.* 14 (1974) 361–370.
49
50 [47] O. Ubbink, R.I. Issa, A method for capturing sharp fluid interfaces on arbitrary meshes, *J.*
51 *Comput. Phys.* 153 (1999) 26–50.
52
53 [48] I. Malgarinos, N. Nikolopoulos, M. Gavaises, Coupling a local adaptive grid refinement
54 technique with an interface sharpening scheme for the simulation of two-phase flow and
55
56
57
58
59
60
61
62
63
64
65

- 1
2
3
4 free-surface flows using VOF methodology, *J. Comput. Phys.* 300 (2015) 732–753.
5
6 [49] V.-T. Nguyen, W.-G. Park, A volume-of-fluid (VOF) interface-sharpening method for
7 two-phase incompressible flows, *Comput. Fluids*. 152 (2017) 104–119.
8
9 [50] T. Waclawczyk, T. Koronowicz, Comparison of CICSAM and HRIC high-resolution
10 schemes for interface capturing, *J. Theor. Appl. Mech.* 46 (2008) 325–345.
11
12 [51] F. Garoosi, T. Mahdi, Presenting a novel higher-order bounded convection scheme for
13 simulation of multiphase flows and convection heat transfer, *Int. J. Heat Mass Transf.* 172
14 (2021) 121163.
15
16 [52] G. Pozzetti, B. Peters, A multiscale DEM-VOF method for the simulation of three-phase
17 flows, *Int. J. Multiph. Flow*. 99 (2018) 186–204.
18
19 [53] M. Dianat, M. Skarysz, A. Garmory, A Coupled Level Set and Volume of Fluid method
20 for automotive exterior water management applications, *Int. J. Multiph. Flow*. 91 (2017)
21 19–38.
22
23 [54] X. Zhang, J. Wang, D. Wan, An improved multi-scale two phase method for bubbly
24 flows, *Int. J. Multiph. Flow*. 133 (2020) 103460.
25
26 [55] H. Wang, H. Wang, F. Gao, P. Zhou, Z.J. Zhai, Literature review on pressure–velocity
27 decoupling algorithms applied to built-environment CFD simulation, *Build. Environ.* 143
28 (2018) 671–678.
29
30 [56] R.I. Issa, Solution of the implicitly discretised fluid flow equations by operator-splitting, *J.*
31 *Comput. Phys.* 62 (1986) 40–65.
32
33 [57] A.J. Chorin, Numerical solution of the Navier-Stokes equations, *Math. Comput.* 22 (1968)
34 745–762.
35
36 [58] D.L. Youngs, Time-dependent multi-material flow with large fluid distortion, *Numer.*
37 *Methods Fluid Dyn.* (1982).
38
39 [59] B.J. Parker, D.L. Youngs, Two and three dimensional Eulerian simulation of fluid flow
40 with material interfaces, Atomic Weapons Establishment, 1992.
41
42 [60] E.G. Puckett, A.S. Almgren, J.B. Bell, D.L. Marcus, W.J. Rider, A high-order projection
43 method for tracking fluid interfaces in variable density incompressible flows, *J. Comput.*
44 *Phys.* 130 (1997) 269–282.
45
46 [61] G.Y. Soh, G.H. Yeoh, V. Timchenko, An algorithm to calculate interfacial area for
47 multiphase mass transfer through the volume-of-fluid method, *Int. J. Heat Mass Transf.*
48 100 (2016) 573–581.
49
50 [62] J.U. Brackbill, D.B. Kothe, C. Zemach, A continuum method for modeling surface
51 tension, *J. Comput. Phys.* 100 (1992) 335–354.
52
53 [63] J.A. Heyns, A.G. Malan, T.M. Harms, O.F. Oxtoby, Development of a compressive
54 surface capturing formulation for modelling free- surface flow by using the volume- of-
55
56
57
58
59
60
61

- fluid approach, *Int. J. Numer. Methods Fluids*. 71 (2013) 788–804.
- [64] P. Cifani, W.R. Michalek, G.J.M. Priems, J.G.M. Kuerten, C.W.M. van der Geld, B.J. Geurts, A comparison between the surface compression method and an interface reconstruction method for the VOF approach, *Comput. Fluids*. 136 (2016) 421–435.
- [65] C.P. Zanutto, E.E. Paladino, F. Evrard, B. van Wachem, F. Denner, Modeling of interfacial mass transfer based on a single-field formulation and an algebraic VOF method considering non-isothermal systems and large volume changes, *Chem. Eng. Sci.* 247 (2022) 116855.
- [66] M. Akhlaghi, V. Mohammadi, N.M. Nouri, M. Taherkhani, M. Karimi, Multi-Fluid VOF model assessment to simulate the horizontal air–water intermittent flow, *Chem. Eng. Res. Des.* 152 (2019) 48–59.
- [67] H. Liu, W. Zhang, M. Jia, Y. He, An improved method for coupling the in-nozzle cavitation with Multi-fluid-quasi-VOF model for diesel spray, *Comput. Fluids*. 177 (2018) 20–32.
- [68] Z. Peng, L. Ge, R. Moreno-Atanasio, G. Evans, B. Moghtaderi, E. Doroodchi, VOF-DEM Study of Solid Distribution Characteristics in Slurry Taylor Flow-Based Multiphase Microreactors, *Chem. Eng. J.* 396 (2020) 124738.
- [69] R.F.L. Cerqueira, E.E. Paladino, F. Evrard, F. Denner, B. van Wachem, Multiscale modeling and validation of the flow around Taylor bubbles surrounded with small dispersed bubbles using a coupled VOF-DBM approach, *Int. J. Multiph. Flow*. 141 (2021) 103673.
- [70] F. Abbas, B. Wang, M.J. Cleary, A.R. Masri, Numerical convergence of volume of fluid based large eddy simulations of atomizing sprays, *Phys. Fluids*. 33 (2021) 42119.
- [71] H.K. Versteeg, W. Malalasekera, *An introduction to computational fluid dynamics: the finite volume method*, Pearson Education, 2007.
- [72] S.-W. Kim, T.J. Benson, Comparison of the SMAC, PISO and iterative time-advancing schemes for unsteady flows, *Comput. Fluids*. 21 (1992) 435–454.
- [73] A. Colagrossi, M. Landrini, Numerical simulation of interfacial flows by smoothed particle hydrodynamics, *J. Comput. Phys.* 191 (2003) 448–475.
- [74] L. Lobovský, E. Botia-Vera, F. Castellana, J. Mas-Soler, A. Souto-Iglesias, Experimental investigation of dynamic pressure loads during dam break, *J. Fluids Struct.* 48 (2014) 407–434.
- [75] Z. Sun, K. Djidjeli, J.T. Xing, Modified MPS method for the 2D fluid structure interaction problem with free surface, *Comput. Fluids*. 122 (2015) 47–65.
- [76] I.M. Jánosi, D. Jan, K.G. Szabó, T. Tél, Turbulent drag reduction in dam-break flows, *Exp. Fluids*. 37 (2004) 219–229.

- 1
2
3
4 [77] P. Jonsson, P. Jonsén, P. Andreasson, T.S. Lundström, J.G.I. Hellström, Modelling dam
5 break evolution over a wet bed with smoothed particle hydrodynamics: A parameter
6 study, *Engineering*. 7 (2015) 248.
7
8 [78] Y. Ye, T. Xu, D.Z. Zhu, Numerical analysis of dam-break waves propagating over dry and
9 wet beds by the mesh-free method, *Ocean Eng.* 217 (2020) 107969.
10
11 [79] A.J. Crespo, M. Gómez-Gesteira, R.A. Dalrymple, Modeling dam break behavior over a
12 wet bed by a SPH technique, *J. Waterw. Port, Coastal, Ocean Eng.* 134 (2008) 313–320.
13
14 [80] Z.H. Gu, H.L. Wen, C.H. Yu, T.W.H. Sheu, Interface-preserving level set method for
15 simulating dam-break flows, *J. Comput. Phys.* 374 (2018) 249–280.
16
17 [81] A. Khoshkonesh, B. Nsom, S. Gohari, H. Banejad, A comprehensive study on dam-break
18 flow over dry and wet beds, *Ocean Eng.* 188 (2019) 106279.
19
20 [82] Z. Ghadampour, M.R. Hashemi, N. Talebbeydokhti, S.P. Neill, A.H. Nikseresht, Some
21 numerical aspects of modelling flow around hydraulic structures using incompressible
22 SPH, *Comput. Math. with Appl.* 69 (2015) 1470–1483.
23
24 [83] J. Yen, C. Lin, C. Tsai, Hydraulic characteristics and discharge control of sluice gates, *J.*
25 *Chinese Inst. Eng.* 24 (2001) 301–310.
26
27 [84] D.R. Basco, A qualitative description of wave breaking, *J. Waterw. Port, Coastal, Ocean*
28 *Eng.* 111 (1985) 171–188.
29
30 [85] P. Liu, J. Gao, Y. Li, Experimental investigation of submerged impinging jets in a plunge
31 pool downstream of large dams, *Sci. China Ser. E Technol. Sci.* 41 (1998) 357–365.
32
33 [86] F. Garoosi, A. Shakibaeinia, Numerical simulation of Rayleigh-Bénard convection and
34 three-phase Rayleigh-Taylor instability using a modified MPS method, *Eng. Anal. Bound.*
35 *Elem.* 123 (2021) 1–35.
36
37 [87] G. Tryggvason, Numerical simulations of the Rayleigh-Taylor instability, *J. Comput.*
38 *Phys.* 75 (1988) 253–282.
39
40 [88] H.-J. Kull, Theory of the Rayleigh-Taylor instability, *Phys. Rep.* 206 (1991) 197–325.
41
42 [89] Y. Chen, P.H. Steen, Suppression of the capillary instability in the Rayleigh–Taylor slot
43 problem, *Phys. Fluids*. 8 (1996) 97–102.
44
45 [90] F. Almasi, M.S. Shadloo, A. Hadjadj, M. Ozbulut, N. Tofighi, M. Yildiz, Numerical
46 simulations of multi-phase electro-hydrodynamics flows using a simple incompressible
47 smoothed particle hydrodynamics method, *Comput. Math. with Appl.* (2019).
48
49 [91] A.C.H. Kruisbrink, F.R. Pearce, T. Yue, H.P. Morvan, An SPH multi- fluid model based
50 on quasi buoyancy for interface stabilization up to high density ratios and realistic wave
51 speed ratios, *Int. J. Numer. Methods Fluids*. 87 (2018) 487–507.
52
53 [92] A. Zainali, N. Tofighi, M.S. Shadloo, M. Yildiz, Numerical investigation of Newtonian
54 and non-Newtonian multiphase flows using ISPH method, *Comput. Methods Appl. Mech.*
55
56
57
58
59
60
61
62
63
64
65

1
2
3
4 Eng. 254 (2013) 99–113.
5

- 6 [93] M. Pang, M. Lu, Numerical study on dynamics of single bubble rising in shear-thinning
7 power-law fluid in different gravity environment, *Vacuum*. 153 (2018) 101–111.
8
9 [94] S.-R. Hysing, S. Turek, D. Kuzmin, N. Parolini, E. Burman, S. Ganesan, L. Tobiska,
10 Quantitative benchmark computations of two- dimensional bubble dynamics, *Int. J.*
11 *Numer. Methods Fluids*. 60 (2009) 1259–1288.
12
13 [95] A. Rahmat, N. Tofighi, M. Yildiz, The combined effect of electric forces and confinement
14 ratio on the bubble rising, *Int. J. Heat Fluid Flow*. 65 (2017) 352–362.
15
16 [96] D. Pan, C. Chang, The capturing of free surfaces in incompressible multi- fluid flows, *Int.*
17 *J. Numer. Methods Fluids*. 33 (2000) 203–222.
18
19 [97] Y. Zhao, H.H. Tan, B. Zhang, A high-resolution characteristics-based implicit dual time-
20 stepping VOF method for free surface flow simulation on unstructured grids, *J. Comput.*
21 *Phys*. 183 (2002) 233–273.
22
23 [98] J. Hua, J. Lou, Numerical simulation of bubble rising in viscous liquid, *J. Comput. Phys*.
24 222 (2007) 769–795.
25
26 [99] Ž. Tuković, M. Perić, H. Jasak, Consistent second-order time-accurate non-iterative PISO-
27 algorithm, *Comput. Fluids*. 166 (2018) 78–85.
28
29 [100] S. MacNamara, G. Strang, Operator splitting, in: *Split. Methods Commun. Imaging, Sci.*
30 *Eng.*, Springer, 2016: pp. 95–114.
31
32 [101] Z. Nasri, A.H. Laatar, J. Balti, Natural convection enhancement in an asymmetrically
33 heated channel-chimney system, *Int. J. Therm. Sci*. 90 (2015) 122–134.
34
35 [102] C. Varsakelis, M. V Papalexandris, A numerical method for two-phase flows of dense
36 granular mixtures, *J. Comput. Phys*. 257 (2014) 737–756.
37
38
39
40
41
42
43
44
45
46
47
48
49
50
51
52
53
54
55
56
57
58
59
60
61
62
63
64
65

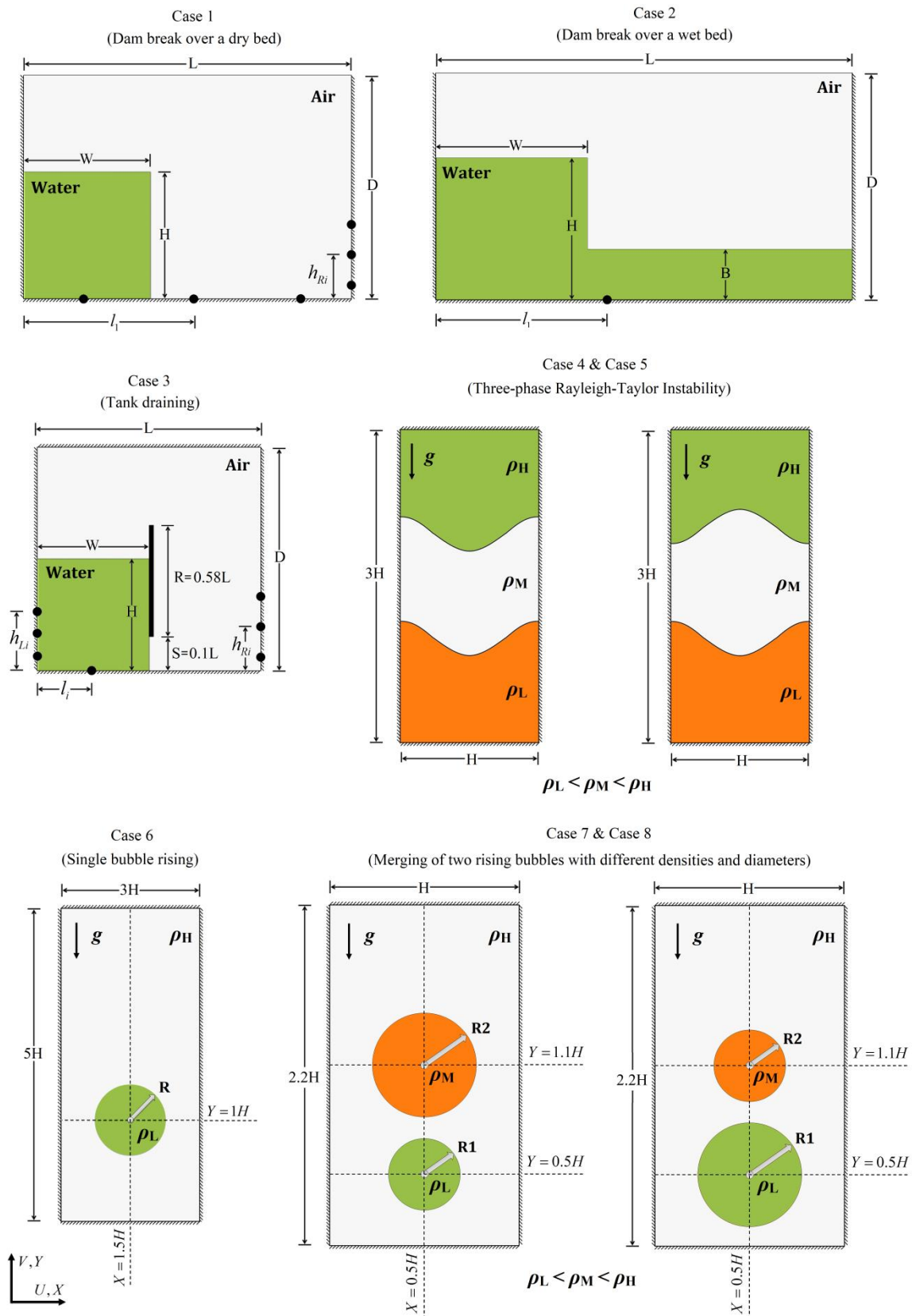


Fig. 1. Schematic diagram of eight different physical models under consideration with associated boundary conditions and coordinate system.

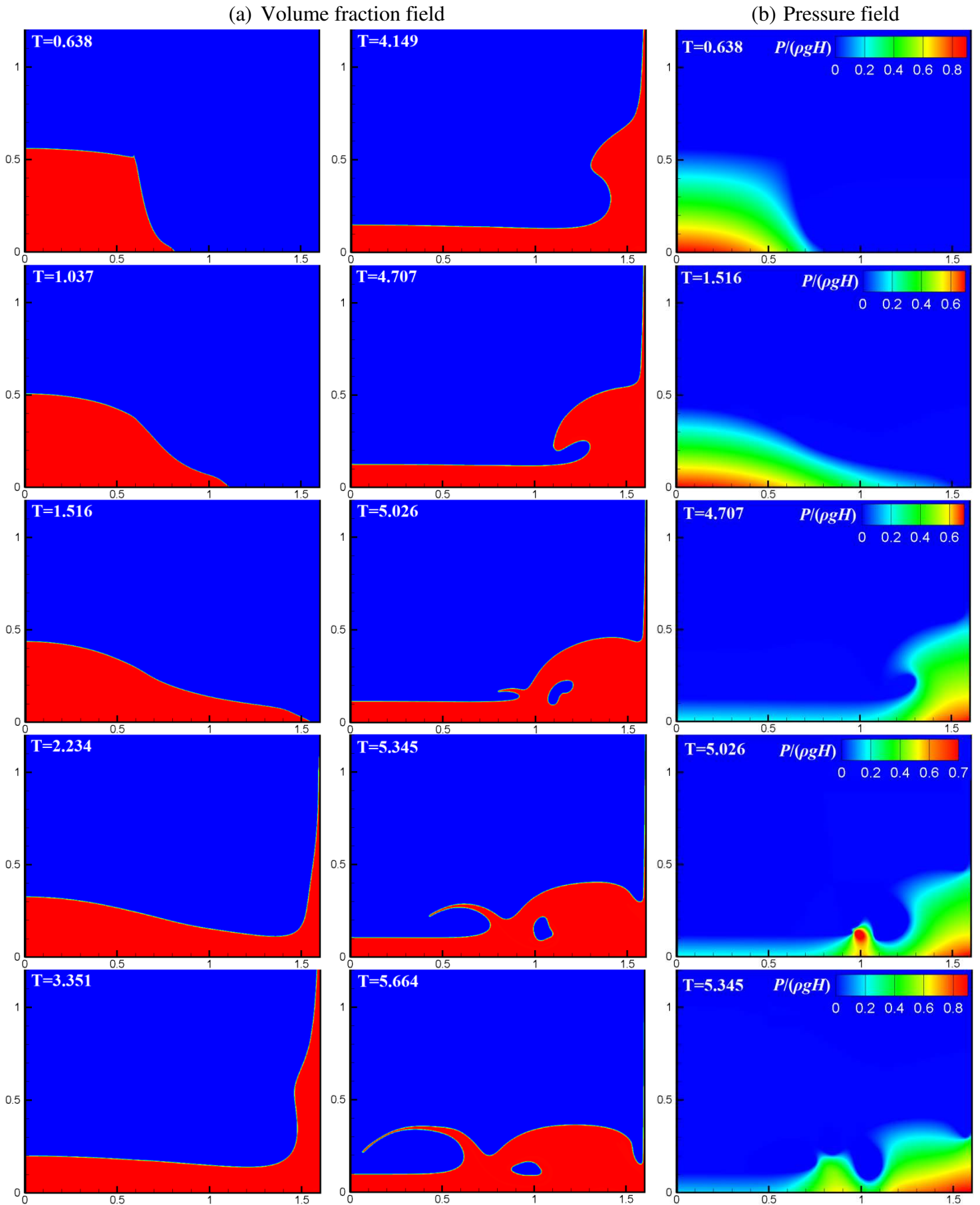


Fig. 2. Time evolution of dam-break flow over a dry bed (case 1) in terms of the volume-fraction and pressure fields calculated in the current work at different time instants.

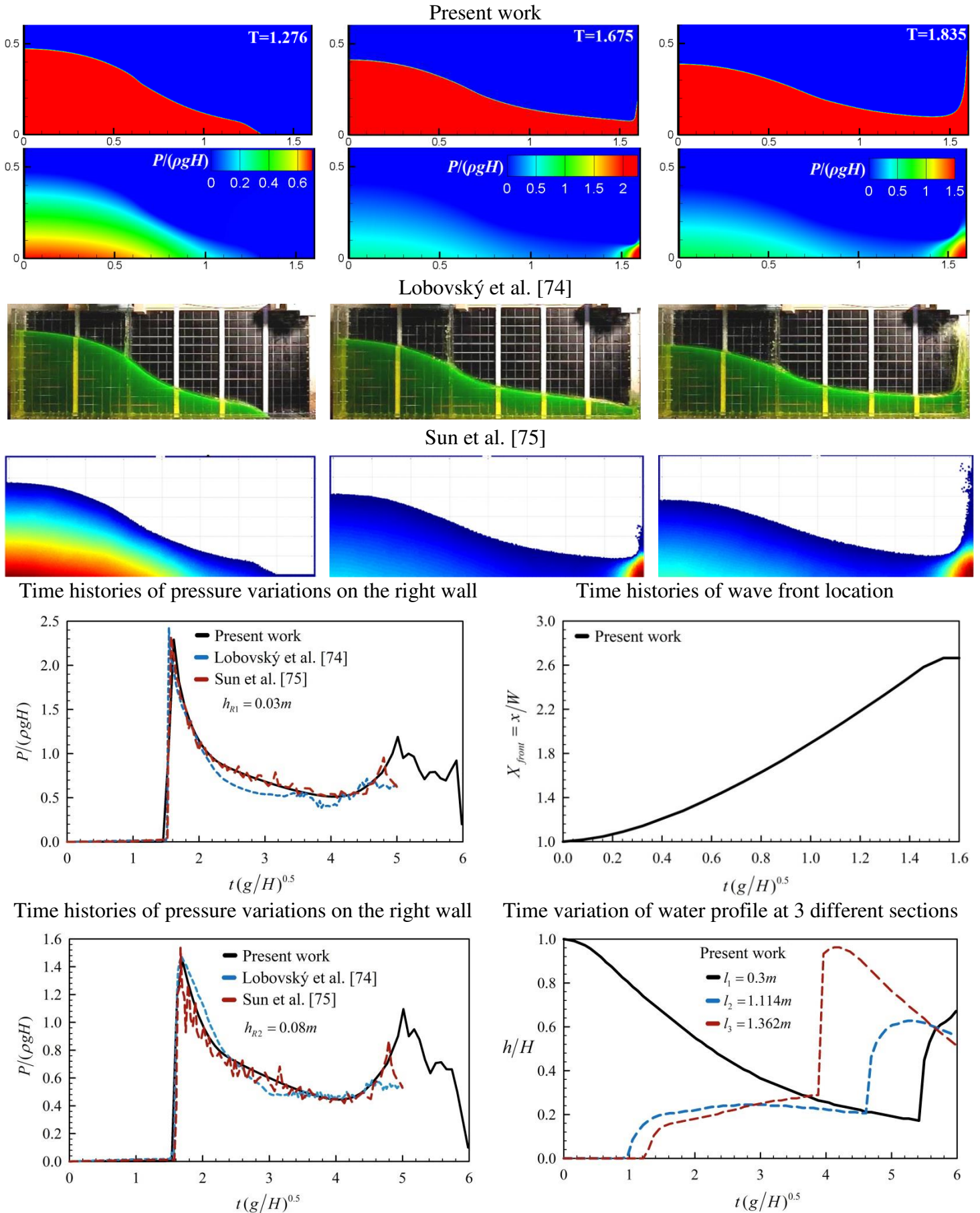


Fig. 3. Qualitative and quantitative comparison of the obtained results with numerical and experimental works of Lobovský et al. [74] and Sun et al. [75] for case 1.

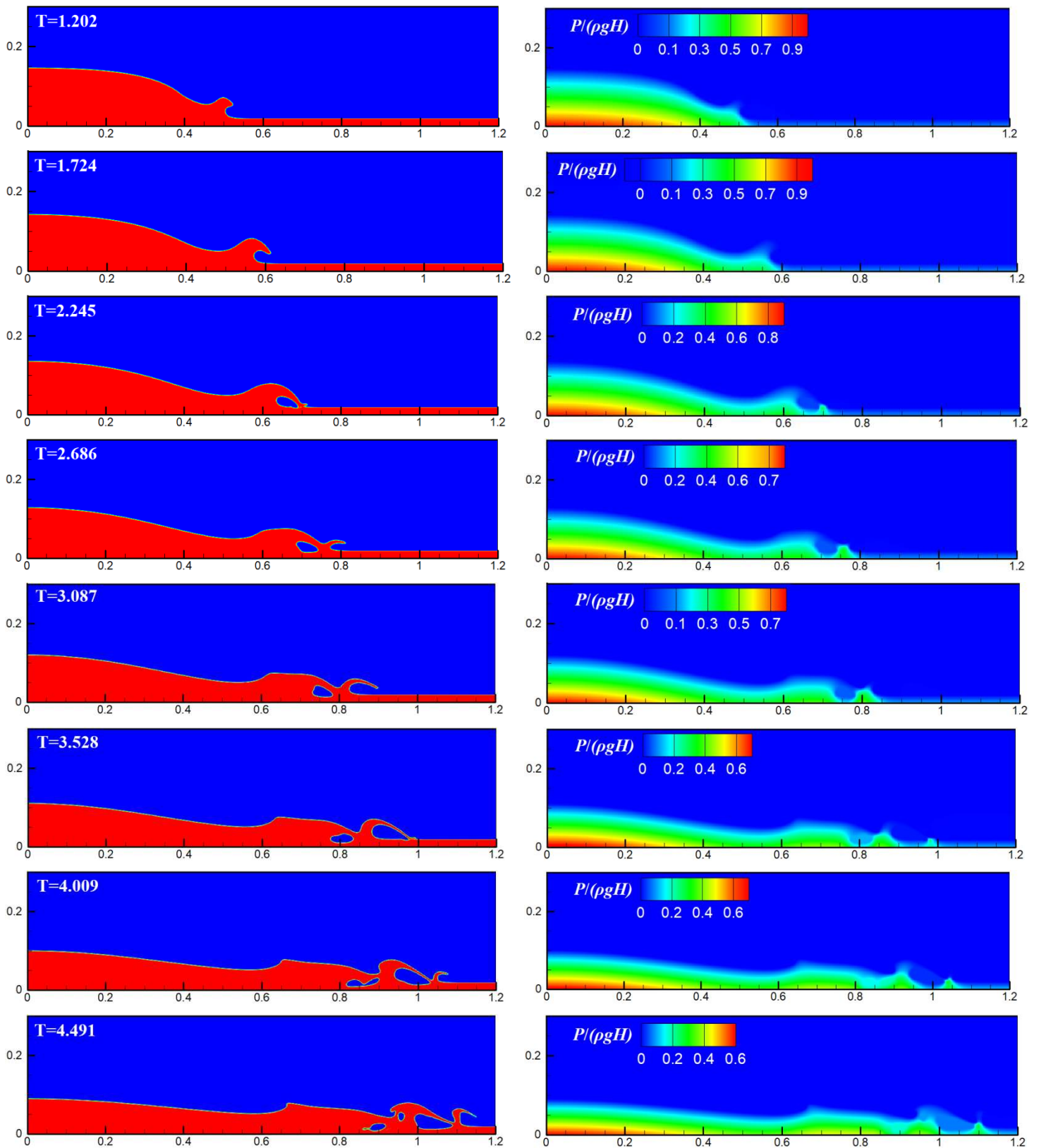
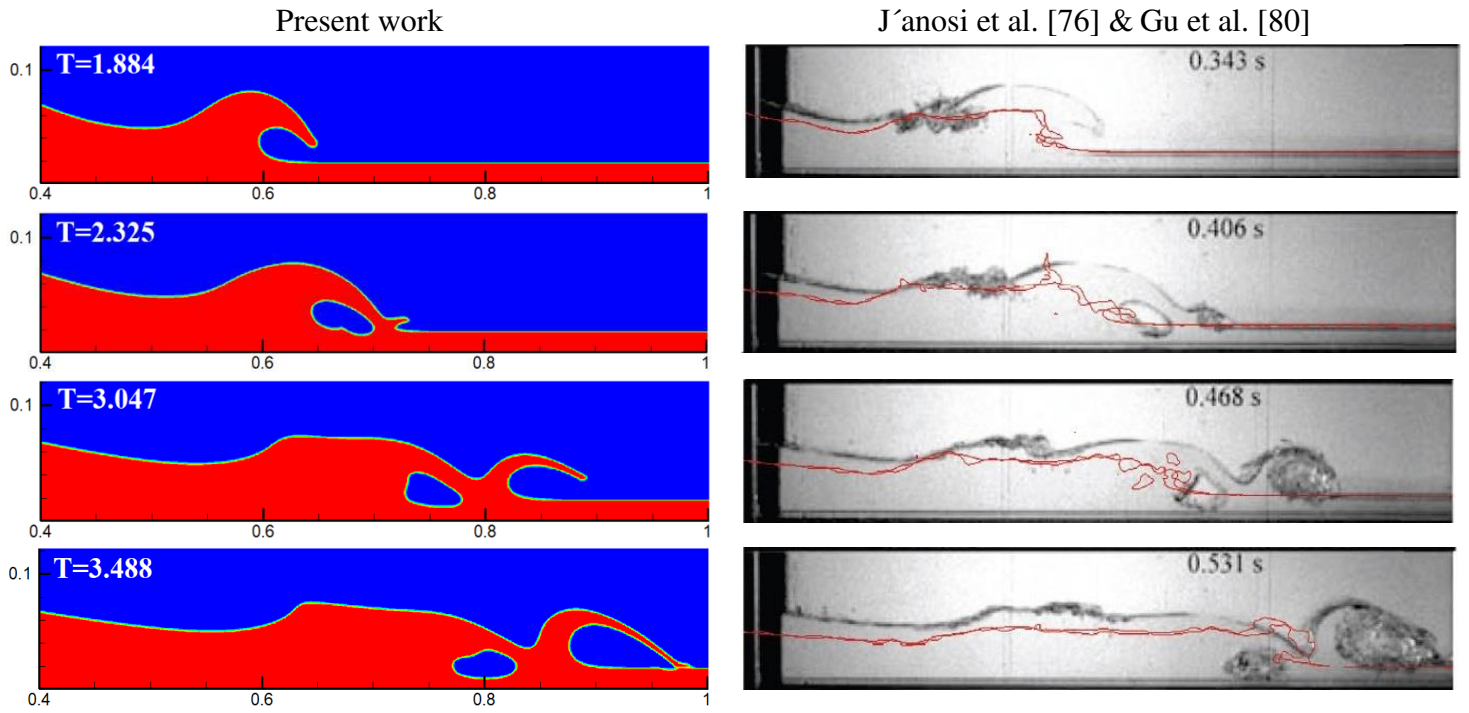
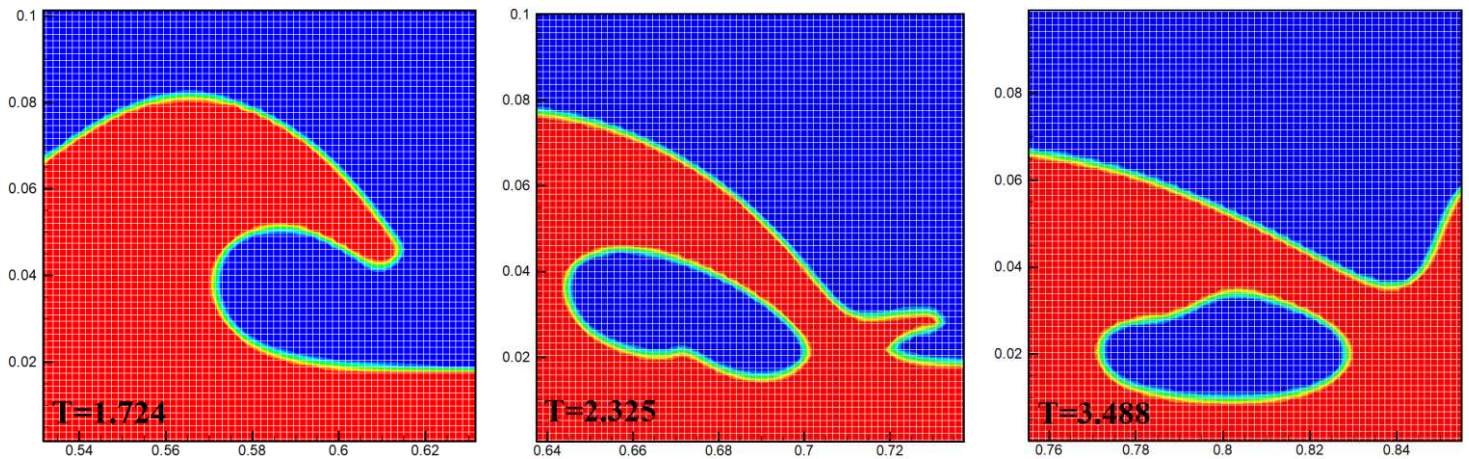


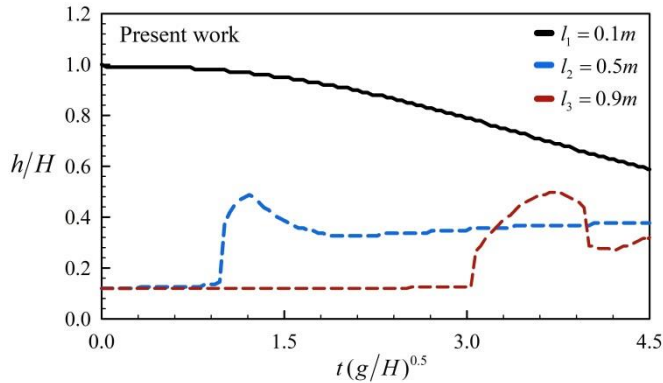
Fig. 4. Time evolution of dam-break flow over a wet bed (case 2) in terms of the volume-fraction and pressure fields calculated in the present work at different time instants.



Enlarged views of the interface at three non-dimensional times



Time histories of water level depth at three different sections ($l_1 = 0.1m$, $l_2 = 0.5m$ and $l_3 = 0.9m$)



Time histories of pressure variations recorded by three different sensors installed on the bottom wall

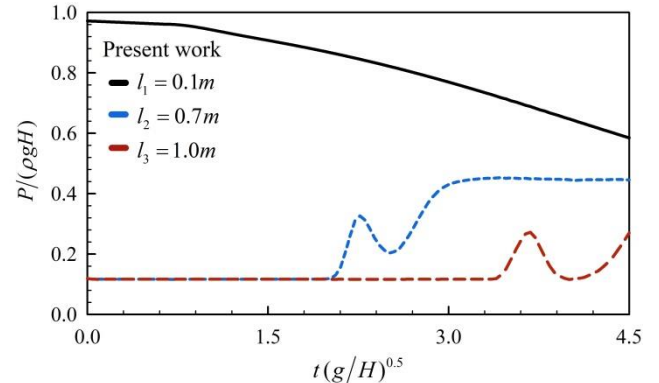


Fig. 5. Qualitative and quantitative comparison of the obtained results with numerical and experimental works of Gu et al. [80] and J'anosı et al. [76] for case 2.

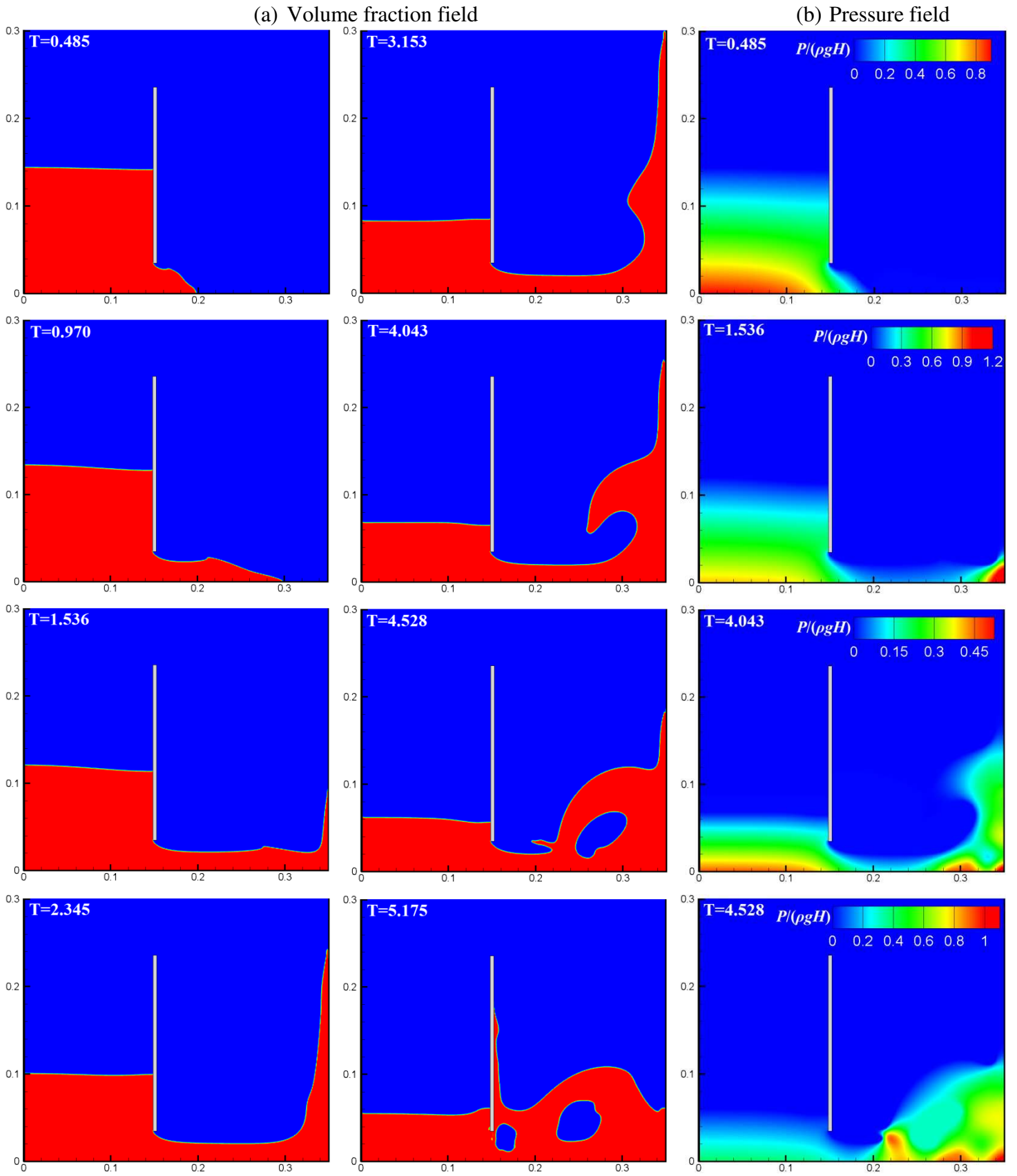


Fig. 6. Time evolution of flow under submerged gate (tank draining, case 3) calculated in the current work at different time instants.

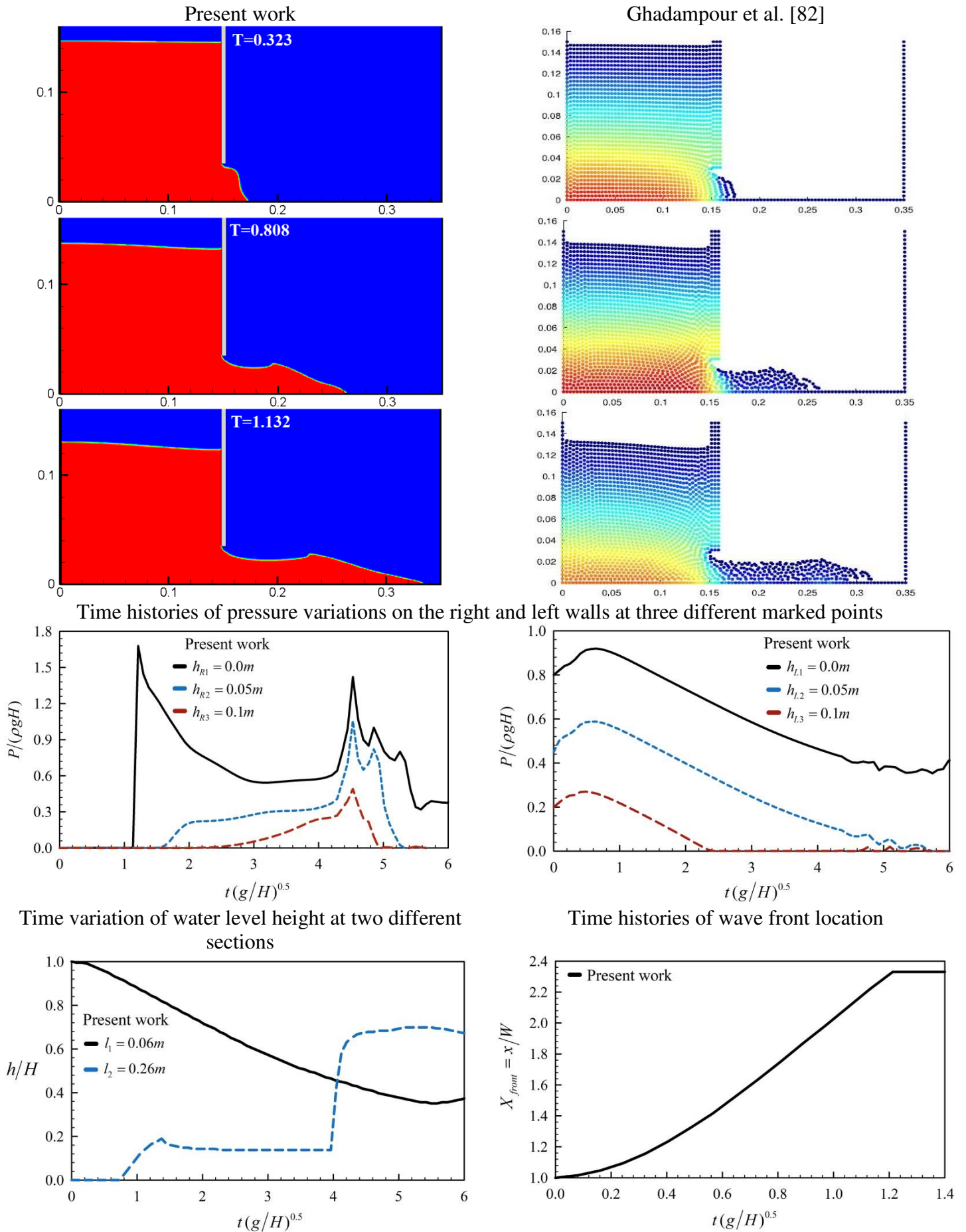


Fig. 7. Qualitative comparison of the obtained results with numerical data of Ghadampour et al. [82] in case 3.

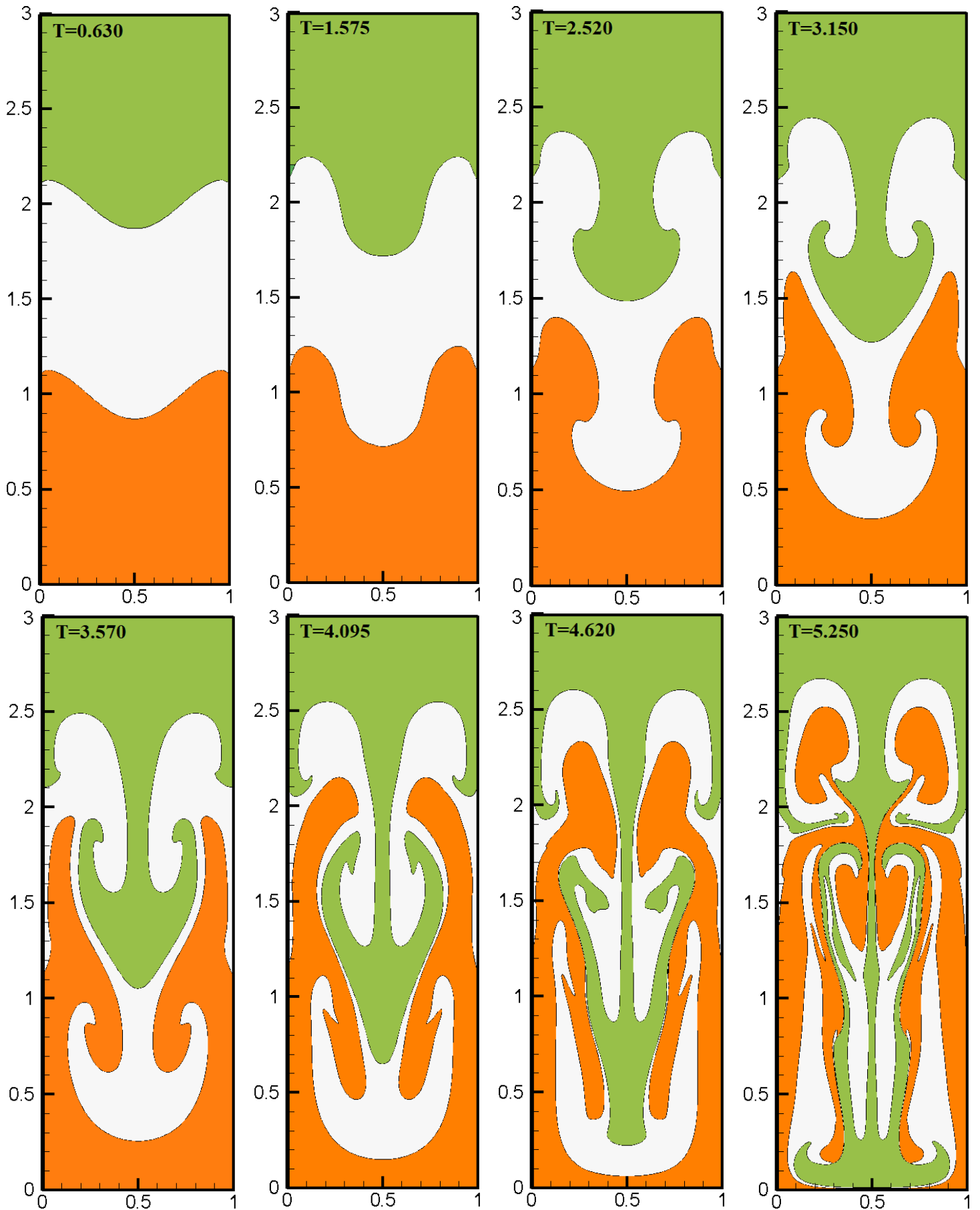


Fig. 8. Time evolution of three-phase Rayleigh-Taylor Instability (case 4) in terms of the volume-fraction field calculated in the current work at different time instants.

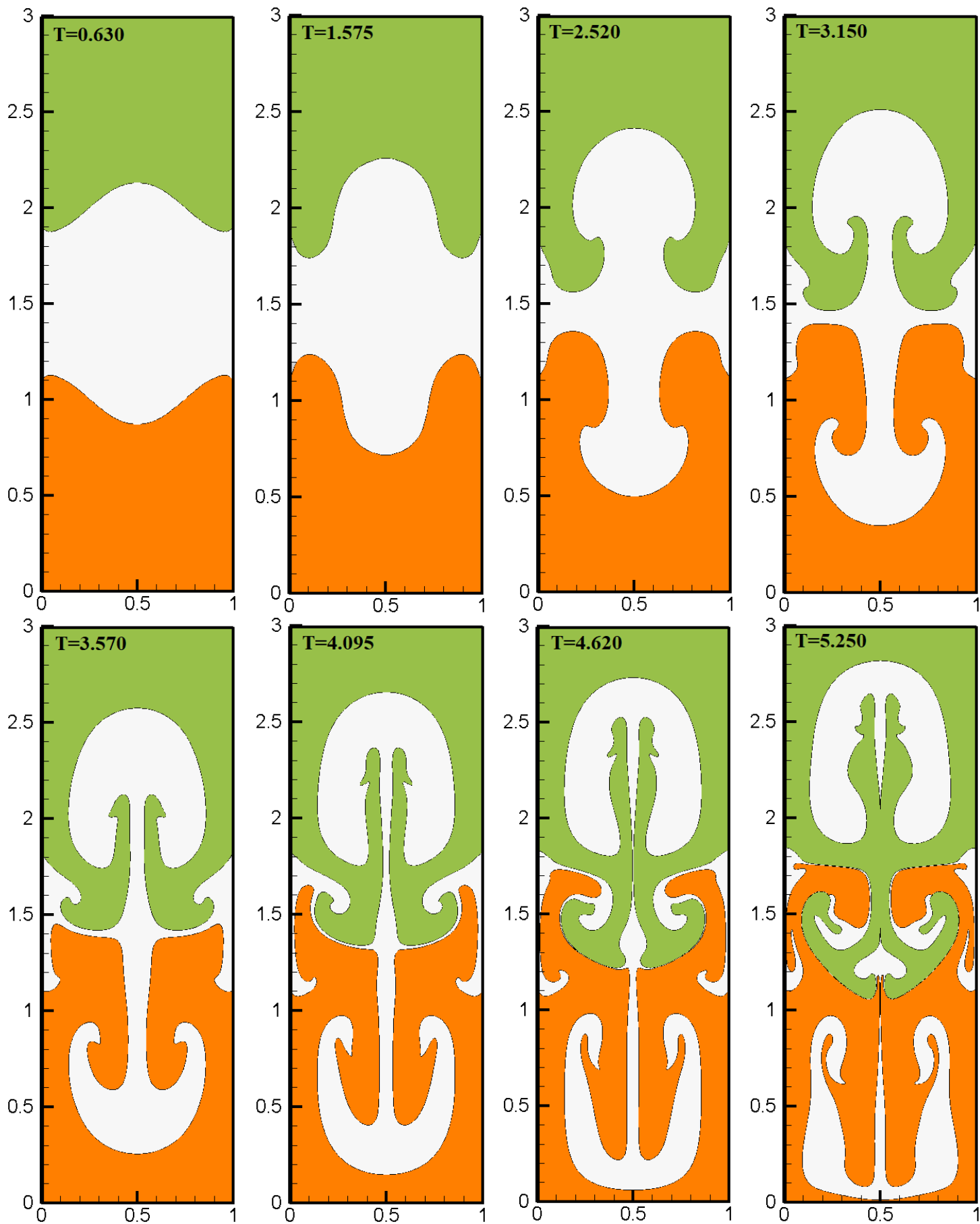


Fig. 9. Time evolution of three-phase Rayleigh-Taylor Instability (case 5) in terms of the volume-fraction field calculated in the current work at different time instants.

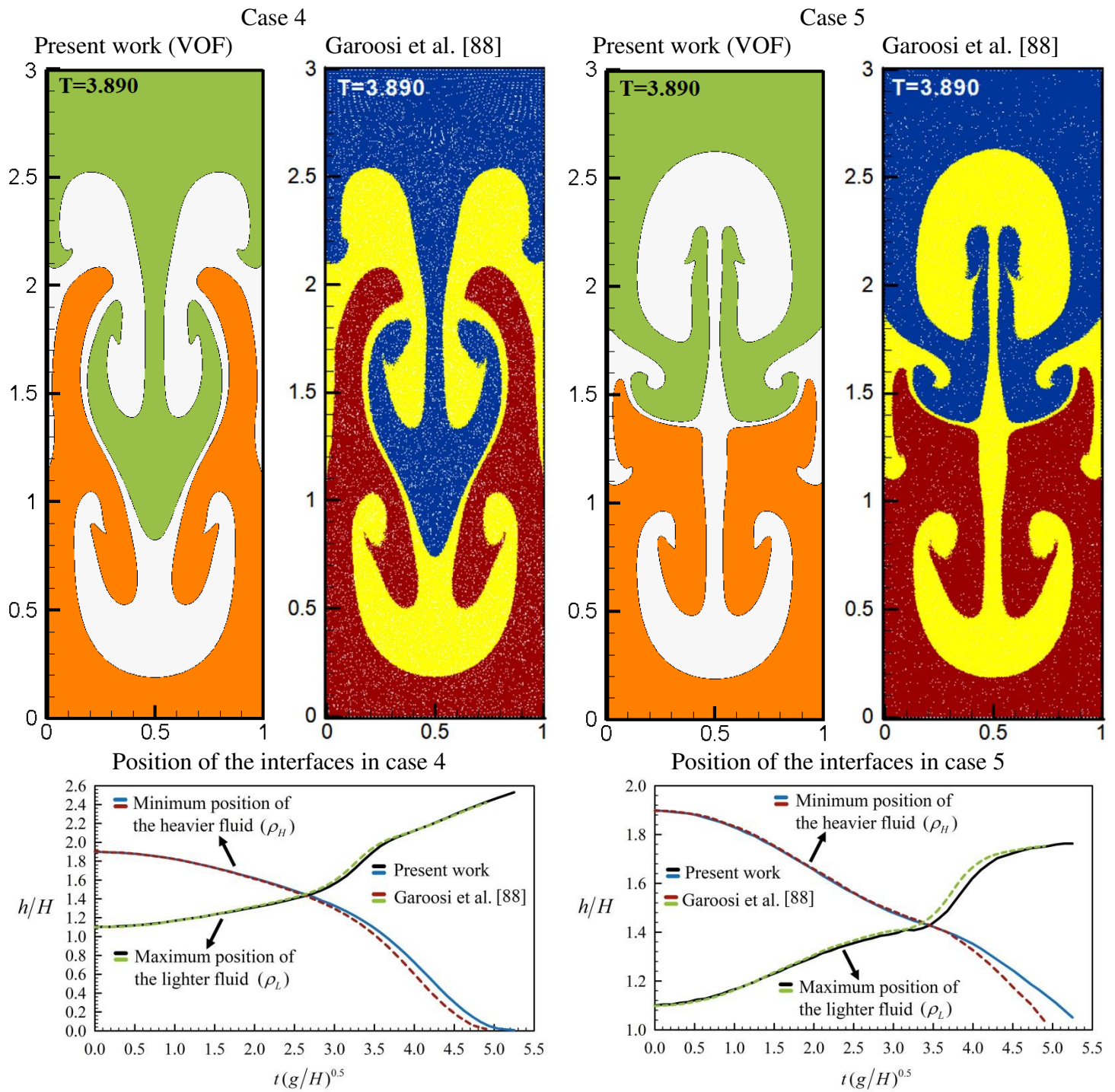
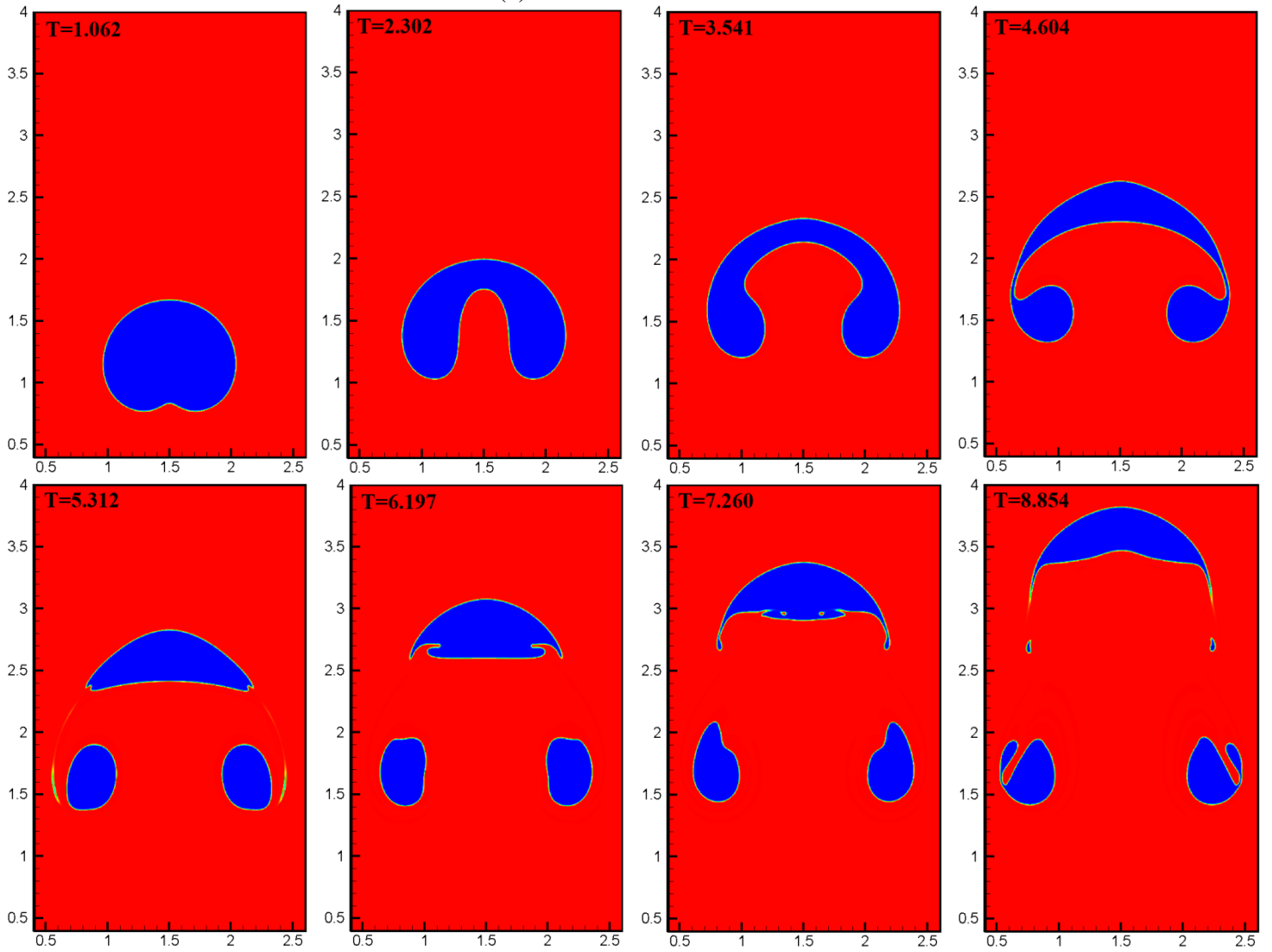


Fig. 10. Qualitative and quantitative comparison of the obtained results with numerical data of Garoosi et al. [88] for cases 4 and 5.

(a) Volume-fraction fields



(b) Pressure fields

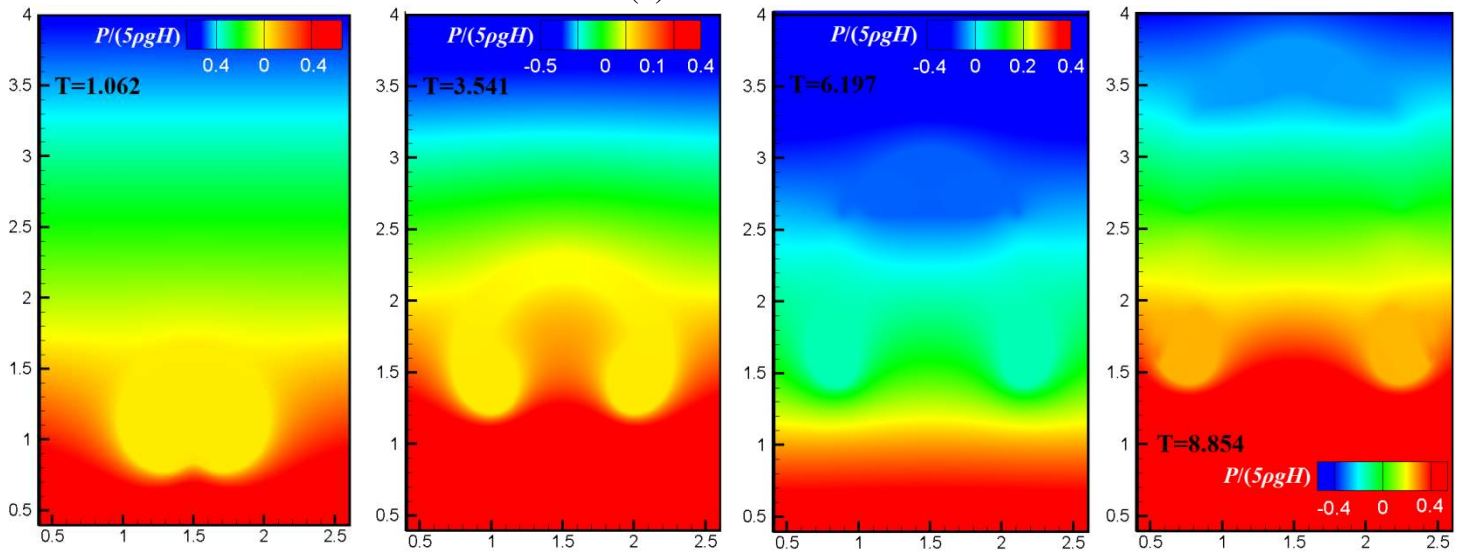


Fig. 11. Time evolution of bubble rising (case 6) in terms of the volume-fraction and pressure fields calculated in the current study at different time instants.

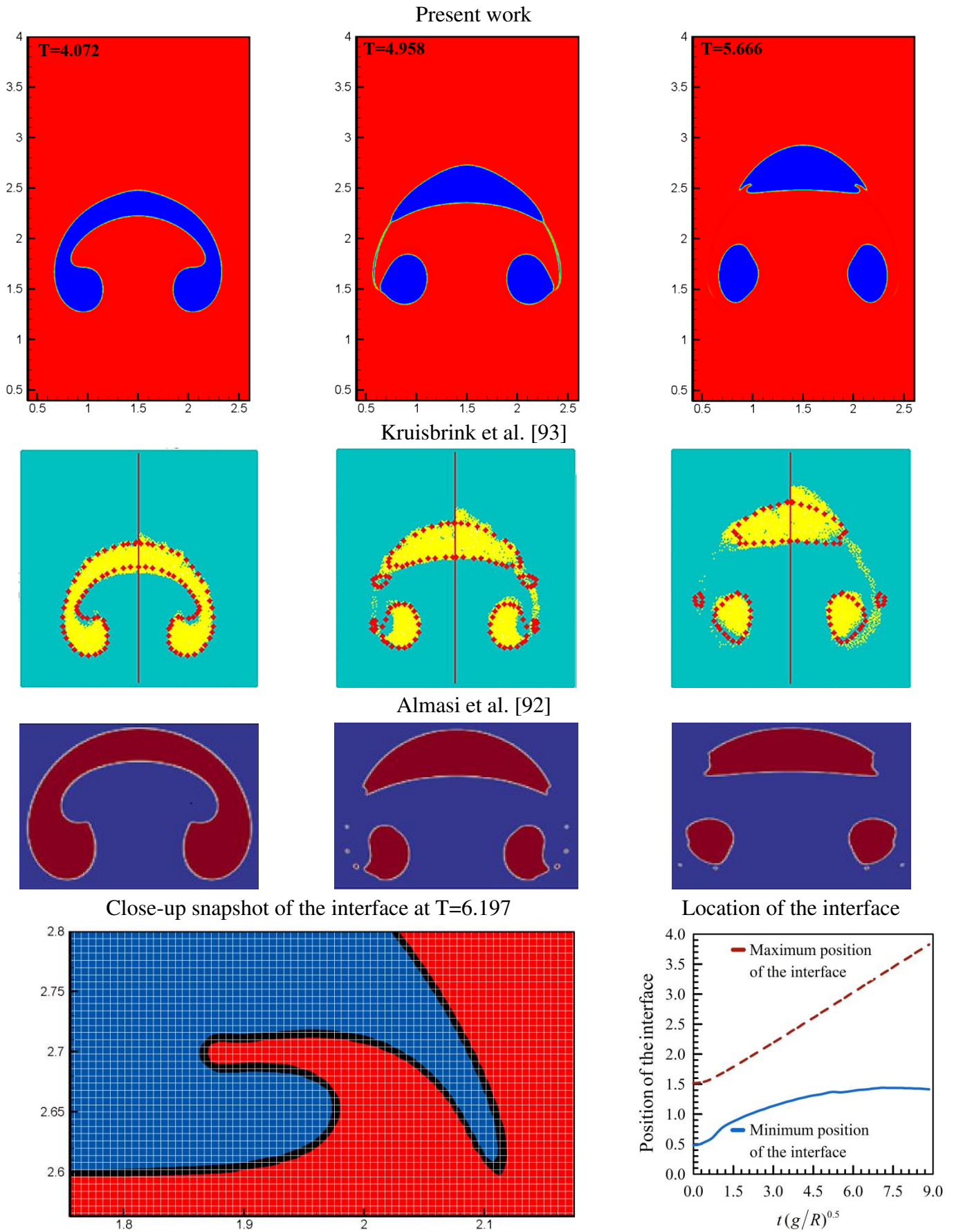


Fig. 12. Qualitative comparison of the obtained results with numerical works of Kruisbrink et al. [93] and Almasi et al. [92] for case 6 at different time instants. Zoomed-in view of the interface together with the time histories of maximum and minimum position of the bubble interface calculated in the current work.

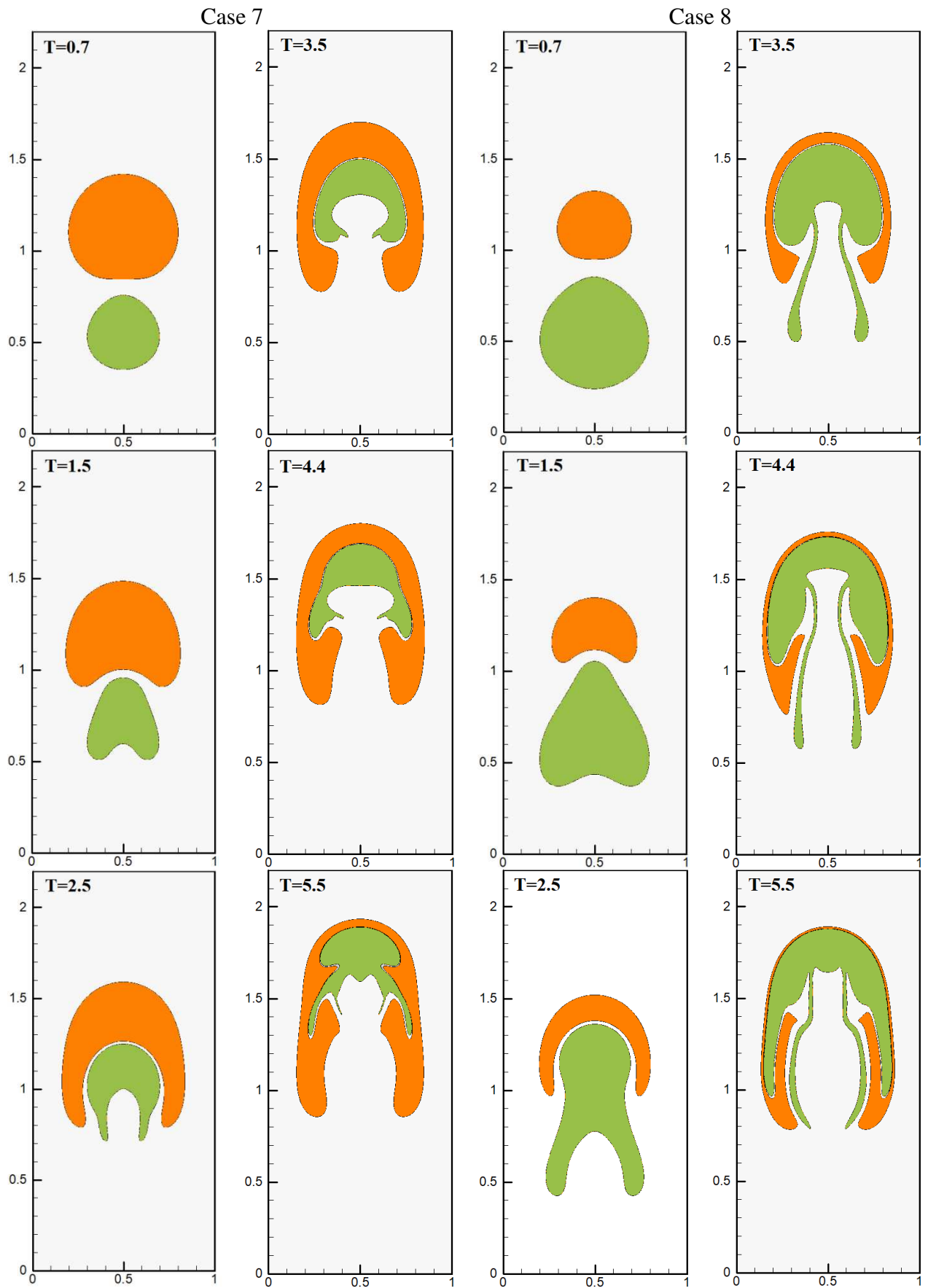


Fig. 13. Transient evolutions of merging of two rising bubbles with different densities (cases 7 & 8) in terms of the volume-fraction fields calculated in the current work at different time instants.

Case 7

Contours of non-dimensional velocity component in x -
direction ($u/\sqrt{g2R_2}$)

Contours of non-dimensional velocity component in
 y -direction ($v/\sqrt{g2R_2}$)

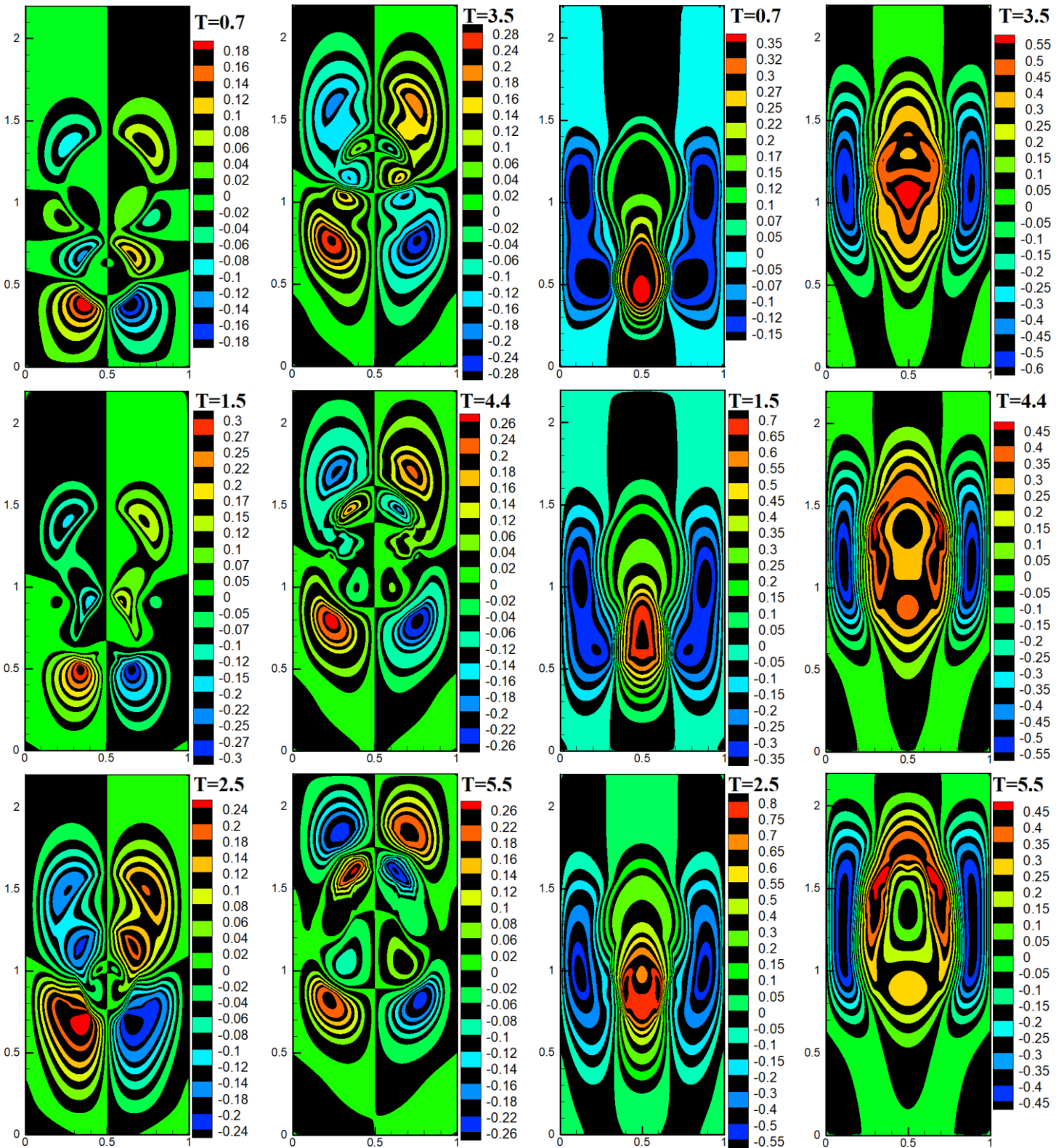


Fig. 14. Contours of non-dimensional velocity in the x and y -directions (u, v) in case 7 at different time instants.

Case 8

Contours of non-dimensional velocity component in x-direction ($u/\sqrt{g2R_1}$)

Contours of non-dimensional velocity component in y-direction ($v/\sqrt{g2R_1}$)

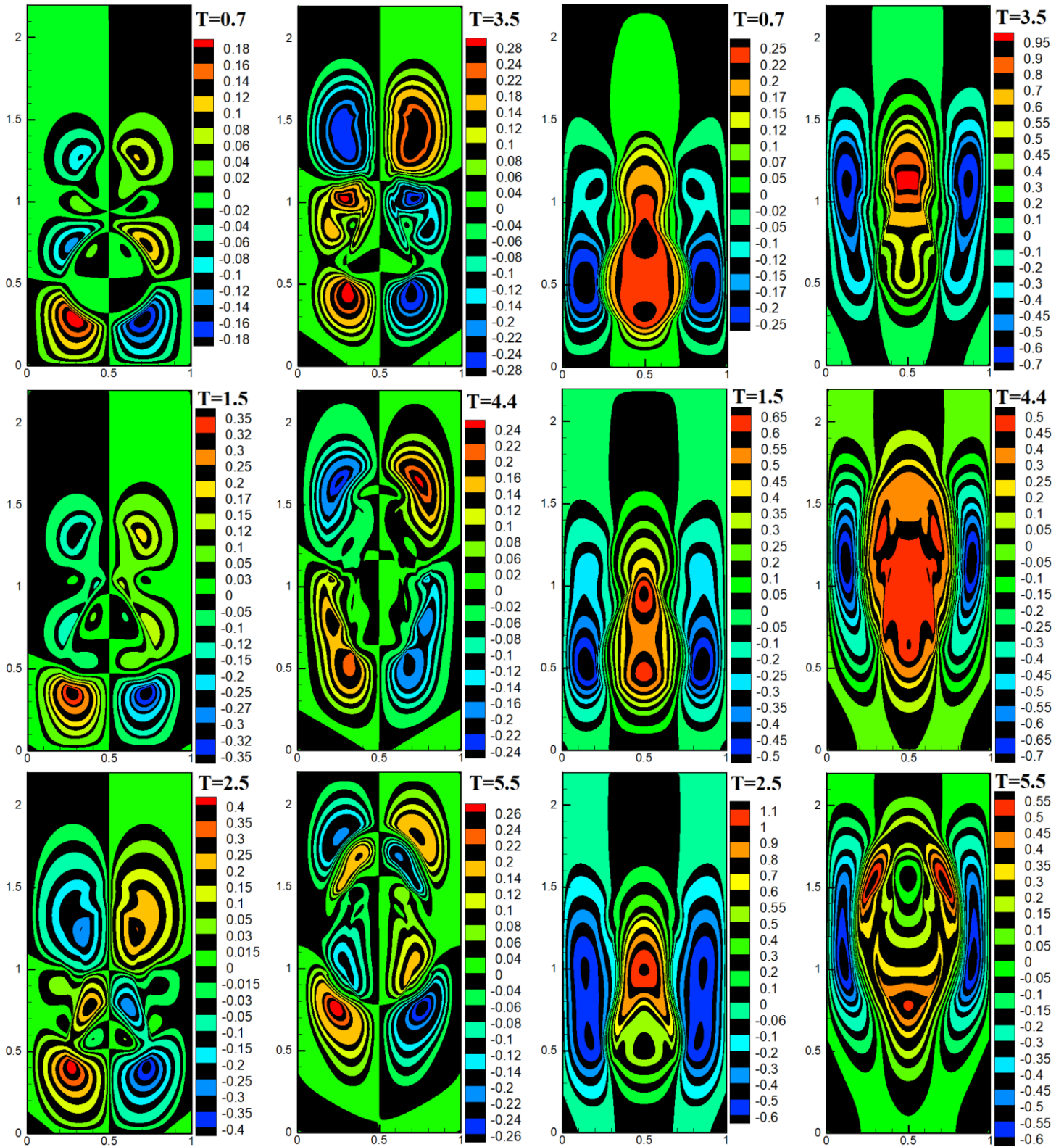


Fig. 15. Contours of non-dimensional velocity in the x and y-directions (u,v) in case 8 at different time instants.

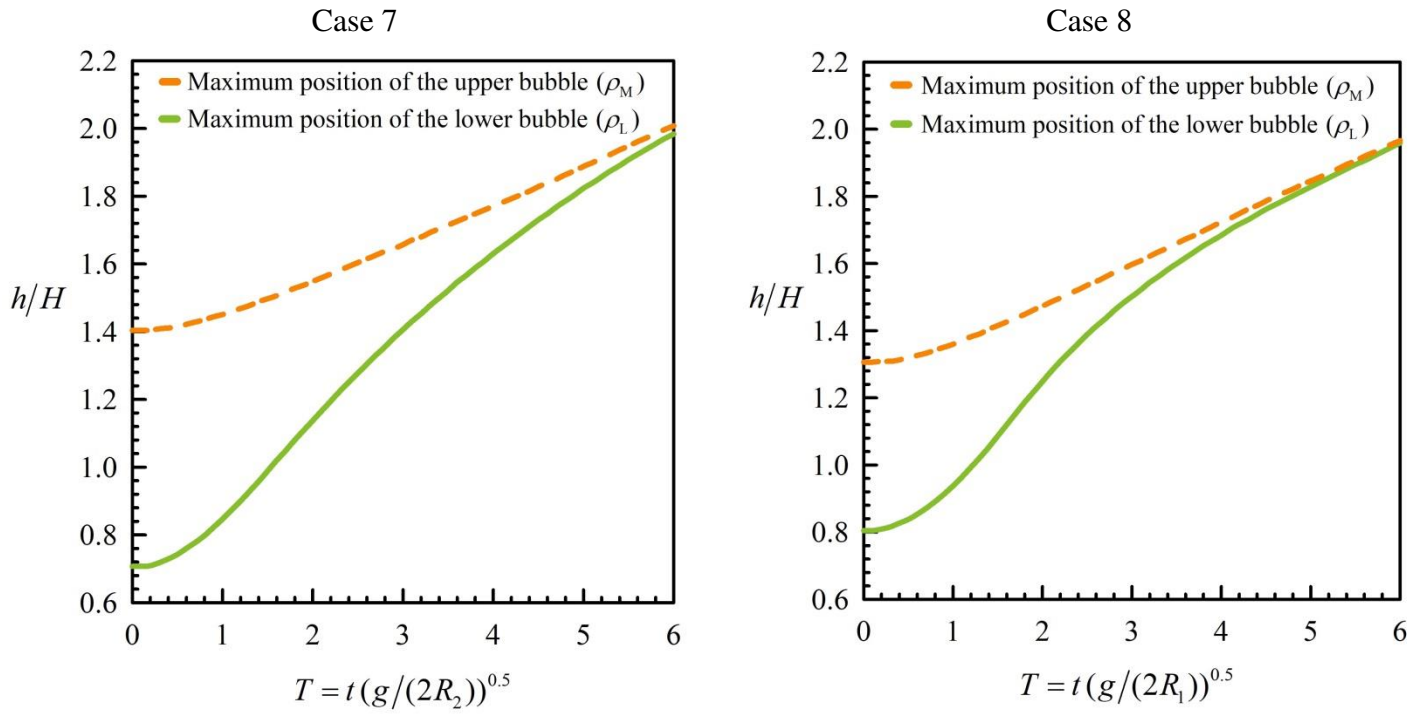
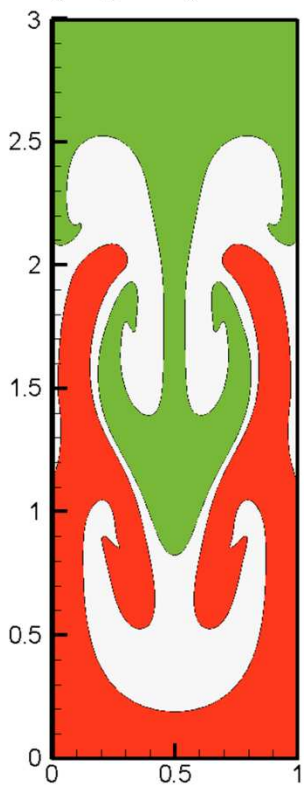


Fig. 16. The time histories of maximum locations of the bubble fronts in cases 7 and 8.

**Three-phase
Rayleigh-Taylor Instability**



Merging of two rising bubbles

